Supplementary Information

Rapid Solution Combustion Synthesis of Ordered Mesoporous Oxide Films with Tunable Architectures: Formation Dynamics Revealed by In Situ GISAXS

Thomas W. Colburn[1,4], Sarah Bindon[1], Hee Won Youn[2], Kuan Liu[1,3], Abigail Carbone[1], Robert D. Miller[1], Reinhold H. Dauskardt[1,*]

[1]Department of Materials Science and Engineering, Stanford University, Stanford, CA 94305

[2]Department of Chemistry, Stanford University, Stanford CA 94305

[3] Now at Exponent, Menlo Park CA, 94025

[4] Now at Meta, Redmond WA, 98052

[*]Correspondence: rhd@stanford.edu

Supplementary Table 1: Summary of In and Ex Situ Precursor Solution Compositions

Precursor Solution Component	Examined Range/Values
Porogen Type	• Pluronic F127 ($PEO_{100}PPO_{65}PEO_{100}$) • Pluronic P123 ($PEO_{20}PPO_{70}PEO_{20}$) • Brij-58 ($C_{16}H_{33}PEO_{20}$)
Porogen:Al^{3+} Molar Ratio	• Pluronic F127: 0.0035, 0.004, 0.0045, 0.005, 0.0055, 0.006 • Pluronic P123: 0.01, 0.013, 0.016, 0.02 • Brij-58: 0.05, 0.075, 0.1
Base:Al^{3+} Molar Ratio	0.1, 0.28, 0.4, 0.56, 0.75
Co-fuel Additive Type (at 0.2 mol co-fuel : mol Al^{3+})	No co-fuel, diglyme, glycolic acid, diglycolic acid, malic acid, citric acid
Aluminum Combustion and Subsequent Anneal Temperature	200 °C, 300 °C, 400 °C, 500 °C
Pre-combustion Annealing Temperature	25 °C, 40 °C, 50 °C, 55 °C, 60 °C, 65 °C, 70 °C, 80 °C, 90 °C
Binary Metal Mixtures	• Cu content: 1%, 10%, 25%, 50% • Ni content: 1%, 10%, 25%, 50% • Li content: 10%, 25%, 50%

Supplementary Section 1: Primer to GISAXS for Mesoporous Thin Film Analysis

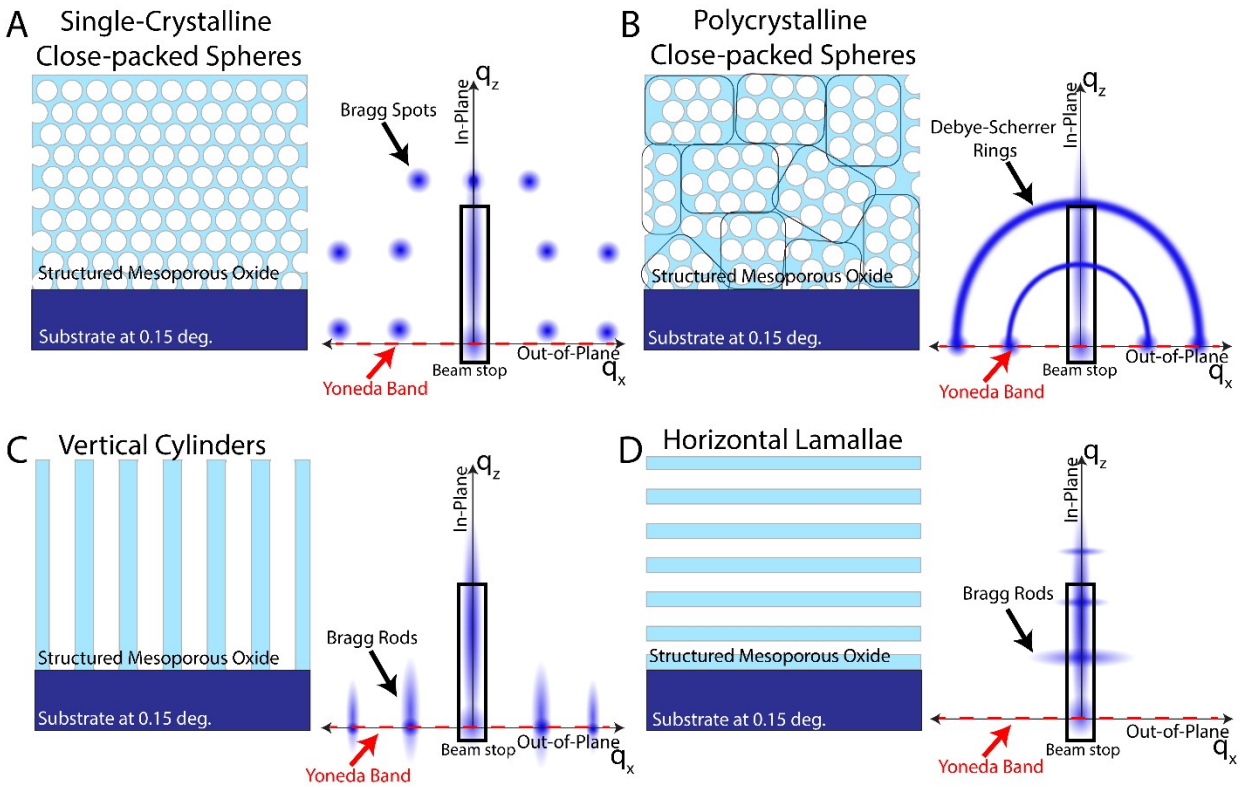

Figure S1: Representative Expected GISAXS Patterns for Mesoporous Oxide Structures A-B) Single and anisotropic, polycrystalline GISAXS pattern showing Bragg spots (A) and Debye-Scherrer rings (B), respectively. C-D) Diffraction from vertical (C) and horizontal (D) structures showing characteristic Bragg rods both out-of-plane and in-plane, respectively. The Yoneda band is labeled in dashed red.

Grazing incidence small-angle X-ray scattering is a powerful technique for measuring mesoscale structures in thin films. For thin film GISAXS, a layer is deposited onto a substrate is exposed to a focused X-ray beam generally from a synchrotron light source or lab-scale X-ray generator at an angle close to the critical angle of the material. The X-rays are then diffracted, scattered, and reflected into a vacuum beam path generally between 1 – 5 meters long. These scattered X-rays are subsequently measured by a 2-dimensional detector. GISAXS provides critical information about film density, structural orientation on the mesoscale, and morphology. Structures within GISAXS can be elucidated by the orientation of the scattering in both the in-plane/parallel to the beam (defined here as q_z) and out-of-plane/perpendicular to the beam (defined here as q_x). Diffraction of the beam occurs when the Bragg-condition is met by the precursor or product oxide periodic structure:

$$n\lambda = 2d\sin(\theta) \qquad \textbf{Equation 1}$$

and the scattering vector relates by way of:

$$q_{xz} = 2\pi/d \qquad \textbf{Equation 2}$$

The overall scattering vector q can be calculated as the norm of the vector with q_x and q_z components.

The contrast of GISAXS on porous media depends directly on the square of the change in density between the pore walls and the pore fill material. In the case of this study, scattering intensity (I) relates to the density changes by the relationship:

$$I(q) \alpha (\rho_{AlOx} - \rho_{Polymer\ Micelle\ or\ Void})^2 \qquad \textbf{Equation 3}$$

This contrast mechanism allows us to both observe both the change in elemental Z contrast and the modification of the matrix structure as both the pore walls form via combustion synthesis and micelles are burned away. Various papers exemplifying GISAXS data, data reduction, and scattering modeling are available for further review.[1–6]

Safety note:

Solution combustion synthesis involves the mixtures of flammable organics and nitrates which, together, result in exothermic reactions. Use caution when handling flammable precursors and avoid combusting large quantities of precursor at one time in a confined reactor.

Supplementary Section 2: F127 Tunable Structures Enabled by Modifying Precursor Chemistry and the PiRO Process

Ex situ GISAXS was performed at SSRL Beamline 1-5 with a 3 m geometry at 15 keV and 0.15 deg incident angle. The films were mounted using vacuum chuck. The entire suite of important parameters for PiRO were analyzed in the beam including curing temperature, porogen amount, co-fuel additives, and base amounts. Transmission FTIR is used to assess through-film carbon contamination remaining post-combustion and the condensation of the matrix at the high wavenumber water peak.

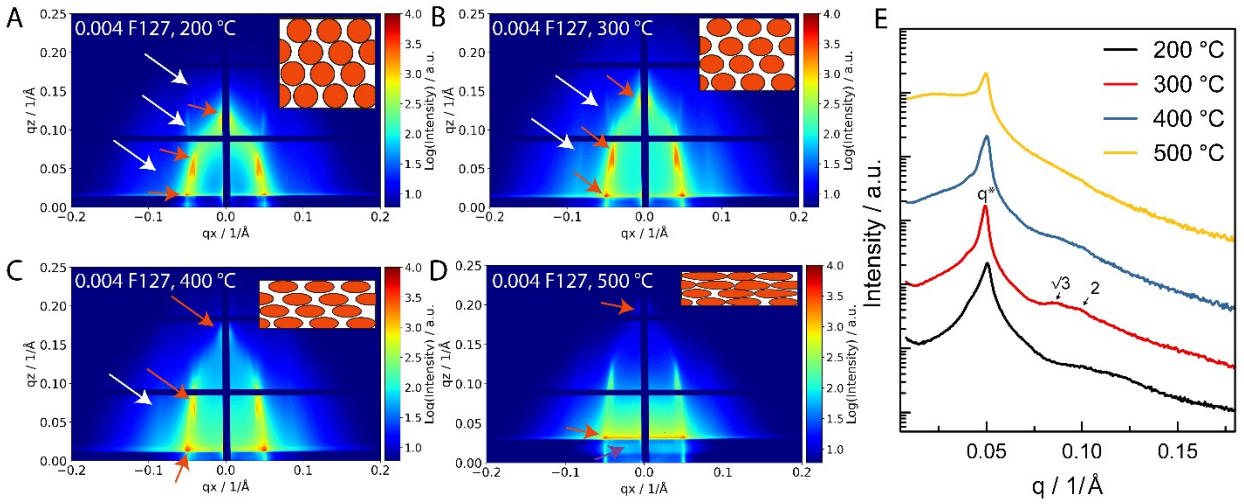

Figure S2: GISAXS of PiRO Alumina Combustion and Subsequent Anneal at Different Temperatures The 2D scattering pattern for a combustion from 200-500 °C (A-D) with a constant 0.004 Pluronic F127: Al^{3+} molar ratio generated with a 5-minute room temperature age and 15 minute 60 °C age before combustion at 200 - 500 °C for 15 minutes. The orange structures provided in the insets are postulated film cross-sectional structures based on the 2D GISAXS pattern. Orange arrows indicate the main out-of-plane, in-plane, and mixed in- and out-of-plane scattering diffraction spots. White arrows indicate higher diffraction orders, and the purple arrow in (D) indicates the collapsed pore feature resulting in increased background. E) 1D line cuts averaged around 5 pixels at the Yoneda band. Main structural peaks are labeled in their approximate locations relative to the main scattering peak q*.

Figure S2D shows a loss in structure due to pore collapse with increased combustion and annealing temperature enabling the formation of confined channels from the close-packed structure. This is observable both in the loss in the diffraction spots at ~0.05 1/Å and an increase in the low q scattering background in **Figure S2E**.

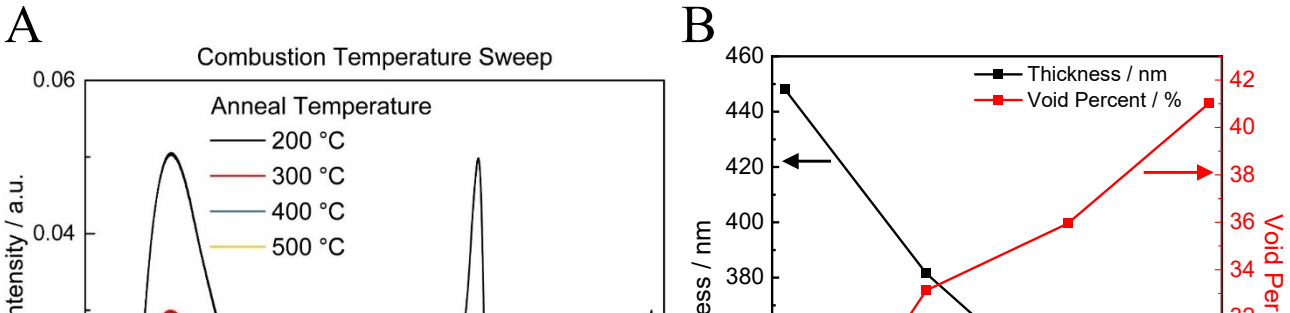

Figure S3: Transmission FTIR of F127 Combustion and Annealing Temperature A) Transmission FTIR showing a loss of water/hydroxides in the water band of 3500 cm^{-1} and a drop in carbonaceous residues at ~1700 cm^{-1} and ~1200 cm^{-1} with increasing annealing temperature. Films were generated with a 5 min room temperature aging step, 15 minute heated aging at 60 °C and combusted and subsequently annealed at 230 °C for 15 minutes. B) Change in film thickness and increase in void content from ellipsometry fittings with increasing combustion temperature.

Sample	L1 Thickness (nm)	+/-	L2 Thickness (nm)	+/-	Layer 1 %Void	+/-	Layer 2 %Void	+/-	X^2	Total Thickness (nm)	Avg Porosity
200 °C	448.1	0.7	-	-	24.2	0.2	-	-	2.1	**448**	**24**
300 °C	279.5	2.4	102.1	4.1	34.9	1.0	28.2	0.3	0.7	**382**	**33**
400 °C	249.8	3.7	86.4	5.6	37.7	1.5	30.8	0.5	1.7	**336**	**36**
500 °C	221.1	3.0	80.0	1.3	45.0	1.3	29.9	0.4	1.3	**301**	**41**

Table S2: Ellipsometric Fits of 0.004 F127 Alumina Varying Combustion and Annealing Temperature

Full details of the ellipsometric fitting are provided in **Supplementary Section 11**.

Figure S4 shows the change in structural motif with Pluronic F127 amount. The structures generated with a precursor of 0.0035, 0.004, 0.0045, 0.0055, and 0.006 all show closed-packed structure while 0.005 shows a characteristic pattern of vertically oriented Bragg rods without closed packing.

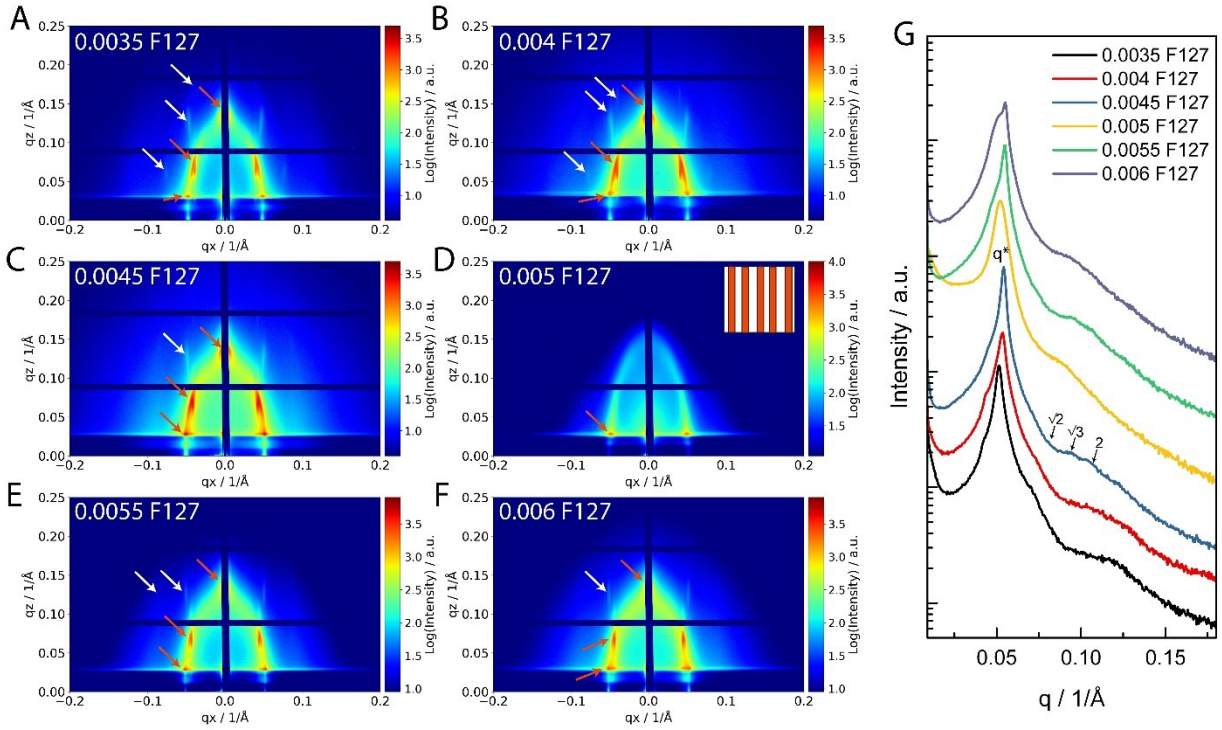

Figure S4: GISAXS of PiRO Alumina Generated with Different Amounts of F127 Porogen The 2D scattering pattern for 0.0035 – 0.006 Pluronic F127: Al^{3+} molar ratios (A-F) generated with a 15-minute room temperature age and 15 minute 60 °C age before combustion at 230 °C. Orange arrows indicate the main out-of-plane, in-plane, and mixed in- and out-of-plane scattering diffraction spots. White arrows indicate higher diffraction orders. G) 1D line cuts averaged around 5 pixels at the Yoneda band.

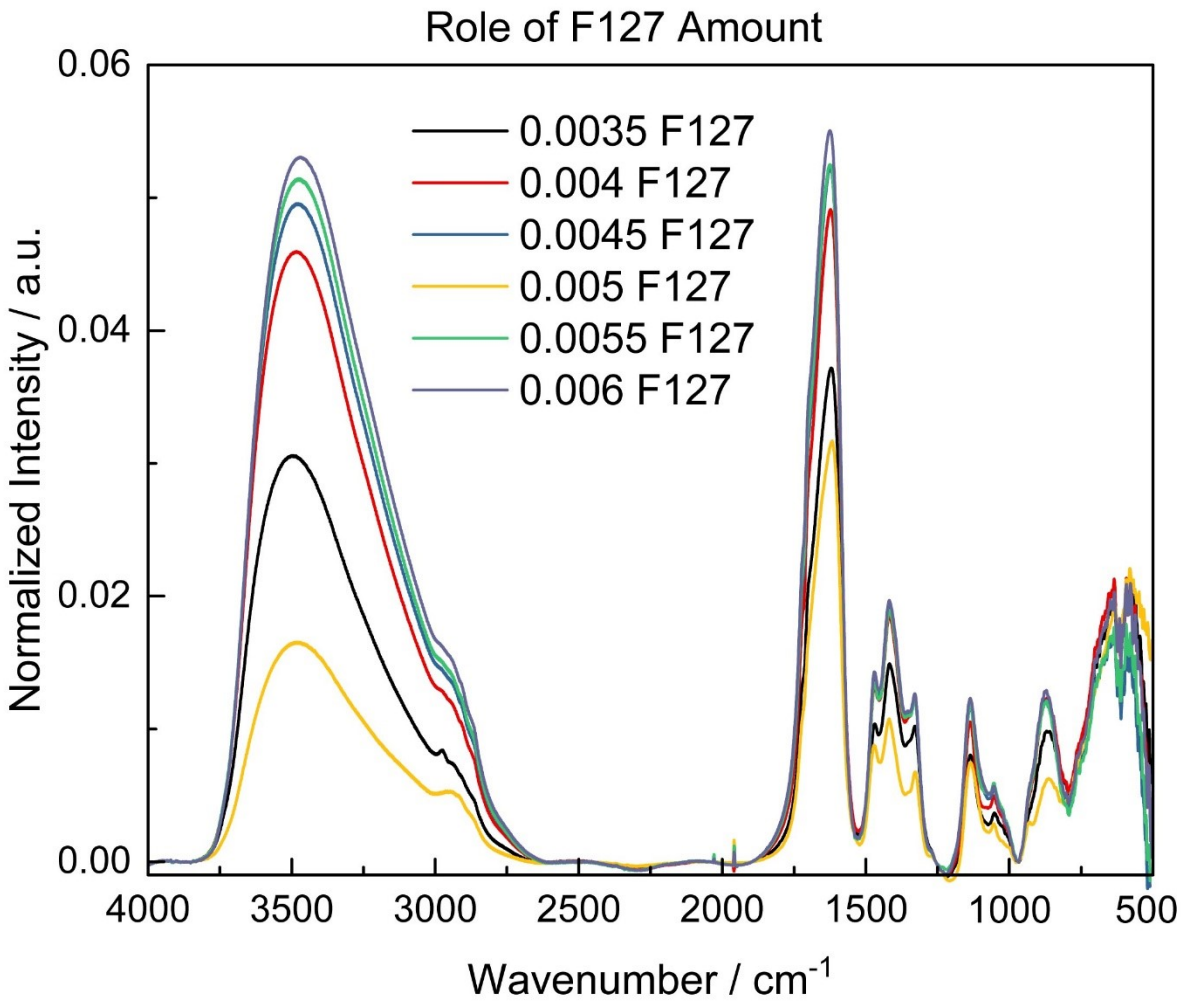

Figure S5: Transmission FTIR of PiRO Films Made With F127 With Various Amounts of F127 The transmission FTIR shows a loss of water/hydroxides in the water band of 3500 cm^{-1} and carbonaceous residues at ~1250-1750 cm^{-1} and ~1000-1250 cm^{-1} with various F127 loadings. The thickness unnormalized data shows increased -OH and carbon residues are present especially in the films with substantial fuel amounts >0.005. Closed packed films all show increased carbon and -OH contributions compared with the vertical rods in 0.005. Films were generated with a 5 min room temperature aging step, 15 minute heated aging at 60 °C and combusted and subsequently cured at 230 °C for 15 minutes.

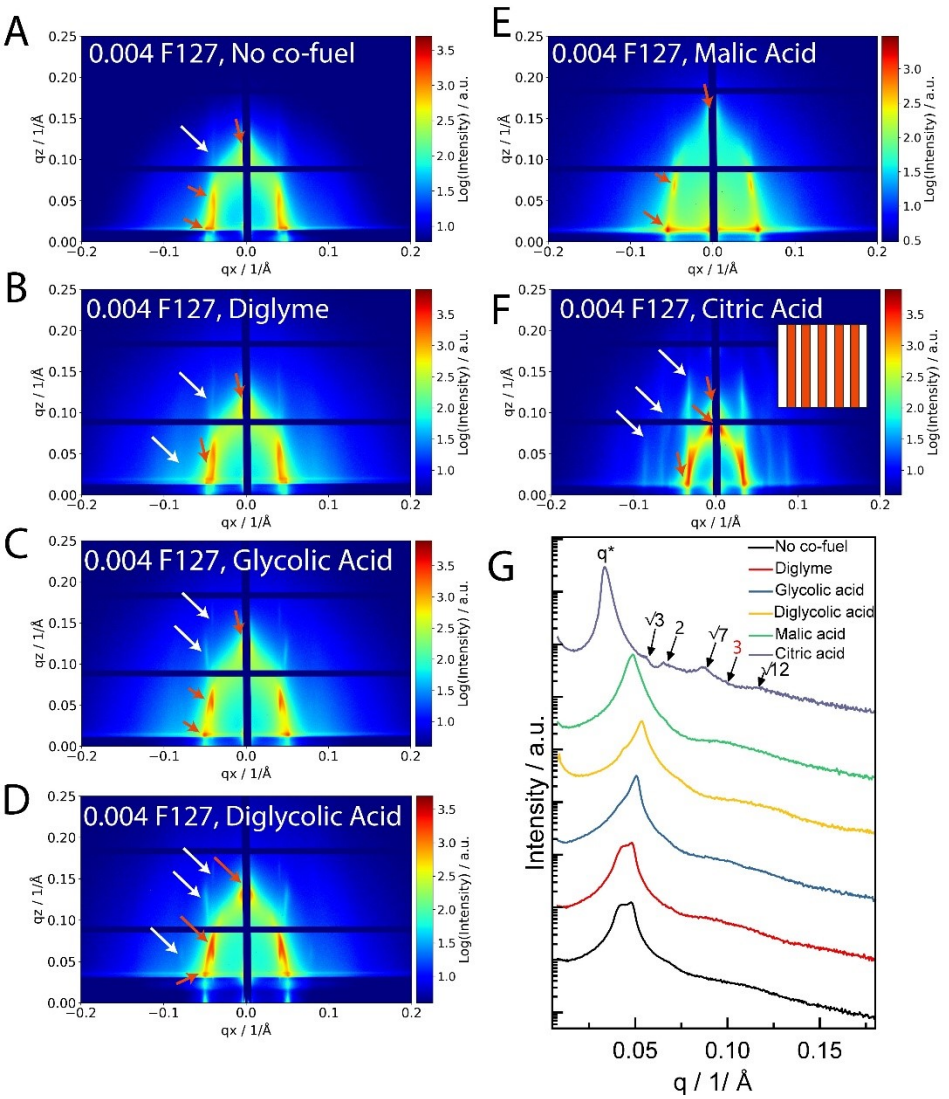

Figure S6: Role of Co-fuel Precursor Additives to Modulate Resulting PiRO Oxide Film Structure 2D GISAXS patterns showing tunable structural motifs resulting from the addition of a co-fuel for a constant 0.004 F127:Al^{3+} ratio. The co-fuels modulate the ligand environment around the aluminum cation and affect the resulting self-assembly process. The absence of co-fuel (A) and use of diglyme (B) show a mixture of ordered pores and disordered (Scherer rings) with disorder indicated as a broad peak at ~0.04 1/Å. Glycolic acid (C), diglycolic acid (D), and malic acid (E) show stronger closed-packing with both vertical and horizontal ordering. Citric acid (F) results in a strongly hexagonally packed film with higher-order diffraction peaks labeled in the 1D Yoneda band line cuts (G). Orange arrows indicate the main out-of-plane, in-plane, and mixed in- and out-of-plane scattering diffraction spots. White arrows indicate higher diffraction orders. Films were generated with a 15 min room temperature aging step, 15 minute heated aging at 60 °C and combusted and subsequently annealed at 230 °C for 15 minutes.

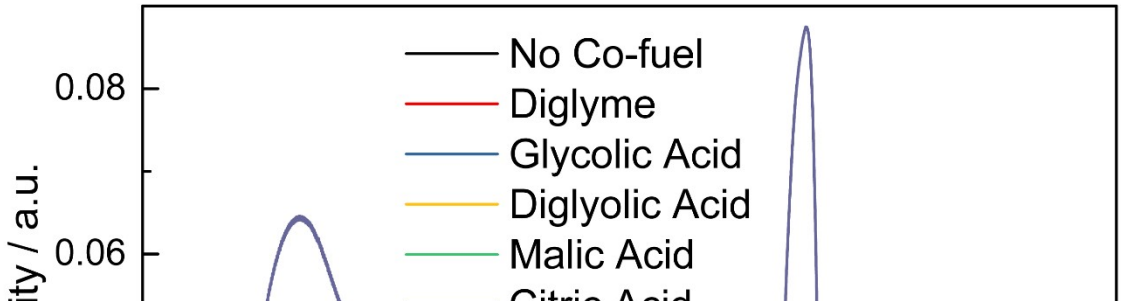

Figure S7: Transmission FTIR of PiRO Films Made With F127 With Various Co-fuels The transmission FTIR shows a loss of water/hydroxides in the water band of 3500 cm^{-1} and carbonaceous residues at ~1250-1750 cm^{-1} and ~1000-1250 cm^{-1} with various co-fuels. Increased -OH and carbon residues are present especially in citric acid films due to a poor oxidation event and the highly oxidized citric acid remaining in the film. Films were generated with a 5 min room temperature aging step, 15 minute heated aging at 60 °C and combusted and subsequently cured at 230 °C for 15 minutes.

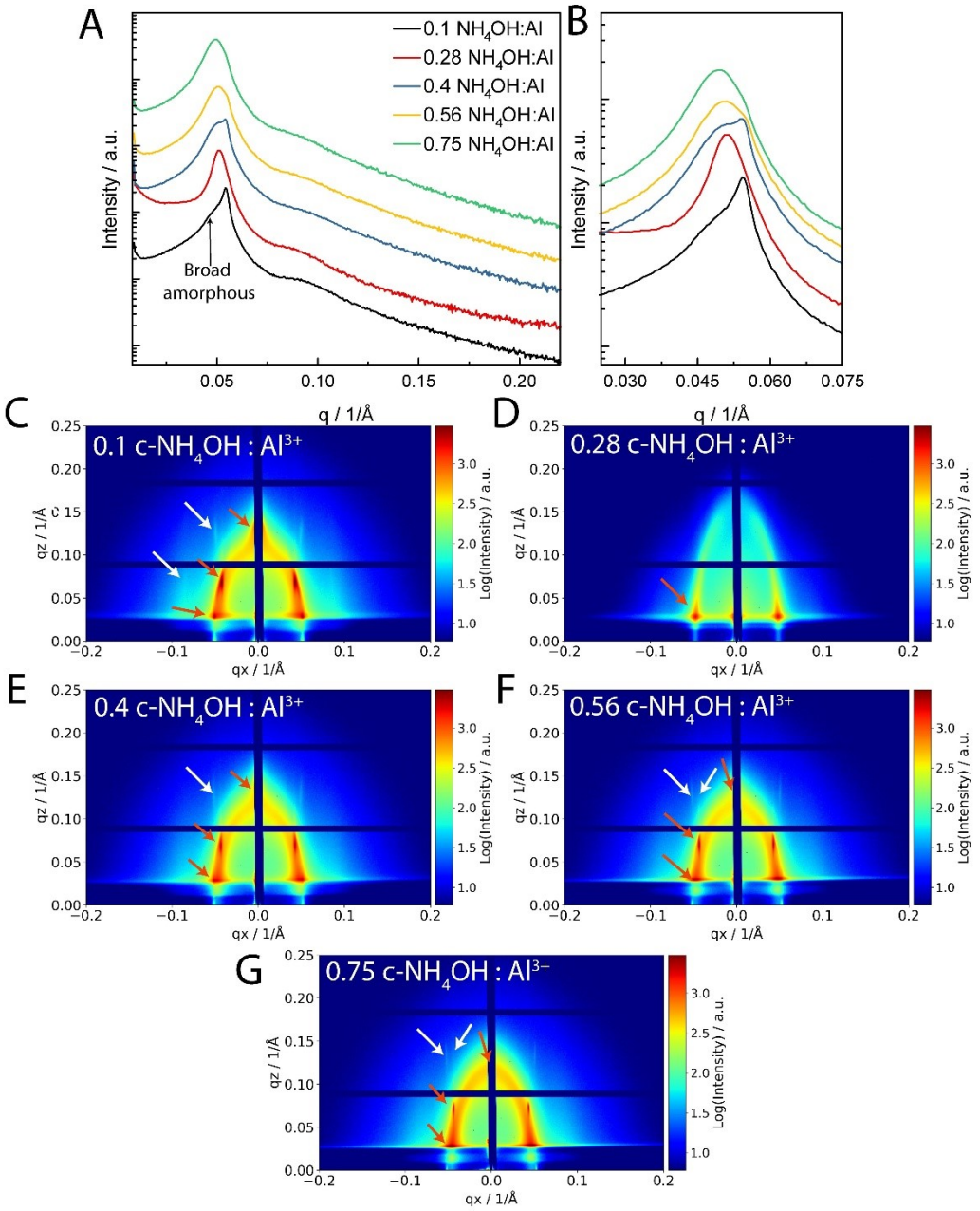

Figure S8: Role of Ammonia to Modulate Resulting PiRO Alumina Film Structure 1D Yoneda band line cuts (A-B) and 2D GISAXS patterns (C-G) for PiRO films with varying ratios of concentrated ammonium hydroxide at a constant Pluronic F127 concentration of 0.005. Films were generated with a 5 min room temperature aging step, 15 minute heated aging at 60 °C and combusted and subsequently annealed at 230 °C for 15 minutes. Orange arrows indicate the main out-of-plane, in-plane, and mixed in- and out-of-plane scattering diffraction spots. White arrows indicate higher diffraction orders.

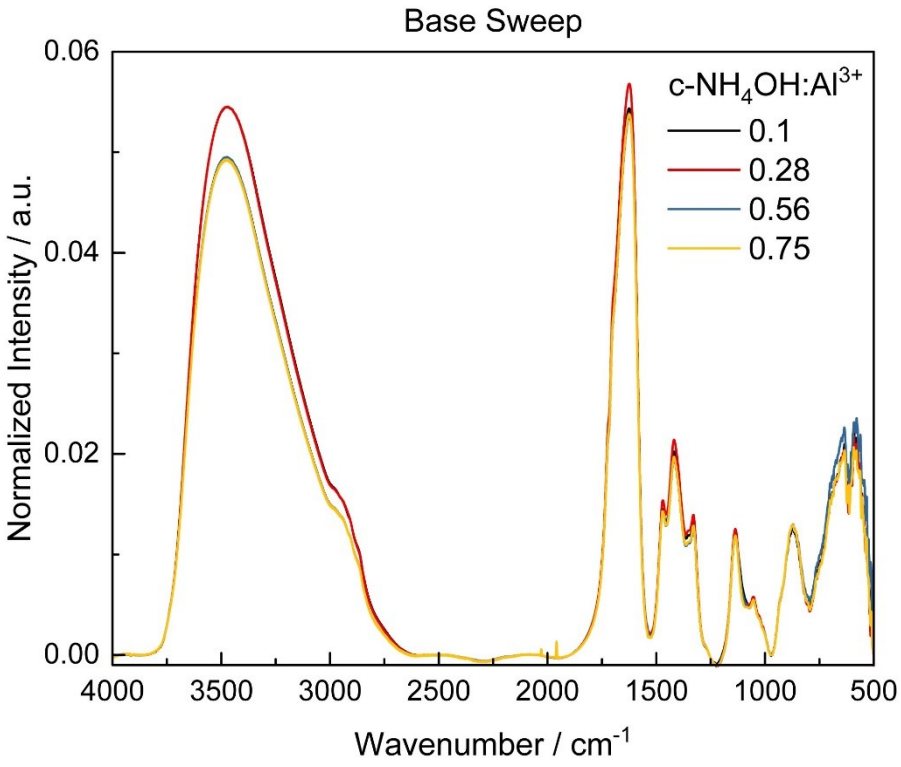

Figure S9: Transmission FTIR of PiRO Alumina Films Made with F127 with Varying Precursor Base Amount The transmission FTIR shows a loss of water/hydroxides in the water band of 3500 cm^{-1} and carbonaceous residues at ~1250-1750 cm^{-1} and ~1000-1250 cm^{-1} with various co-fuels. Increased -OH and carbon residues are present especially in citric acid films due to a poor oxidation event and the highly oxidized citric acid remaining in the film. Films were generated with a 5 min room temperature aging step, 15 minute heated aging at 60 °C and combusted and subsequently annealed at 230 °C for 15 minutes.

Supplementary Section 3: P123 Tunable Alumina Structures Enabled by Modifying Precursor Chemistry and the PiRO Process

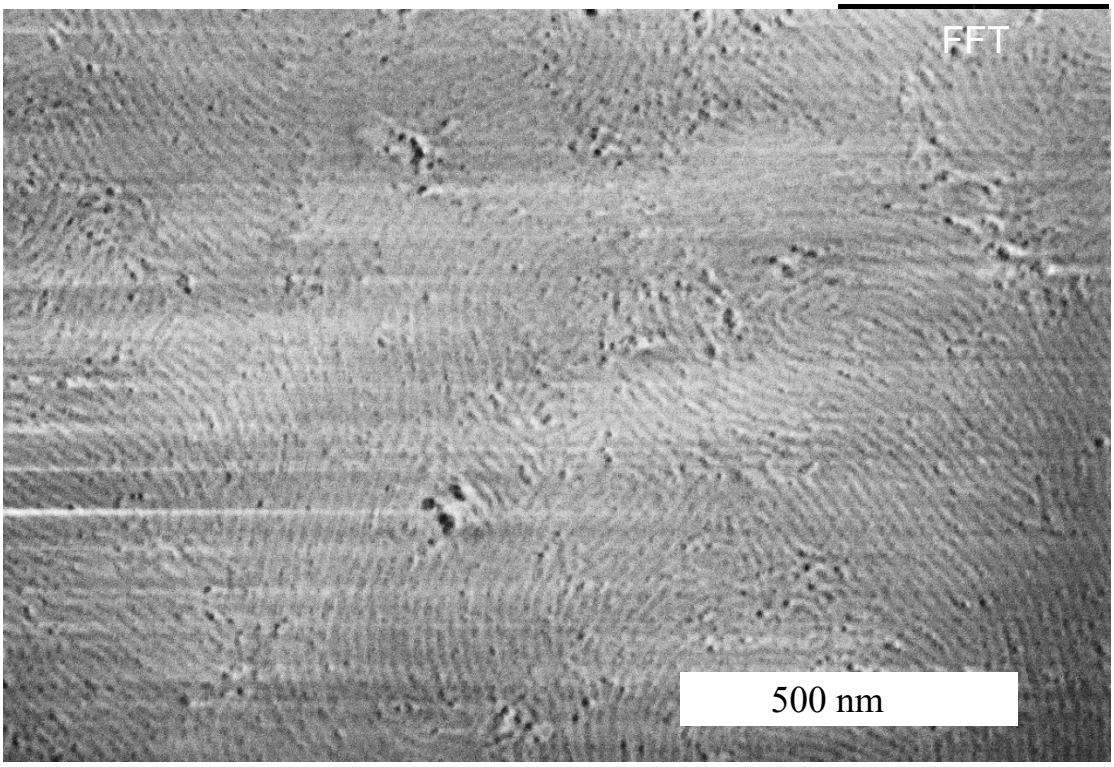

Figure S10: P123 PiRO Film Resulting in Worm-like Chain Pore Structure SEM showing packed, worm-like chain structures in the mesoporous alumina. The inset shows the SEM image FFT.

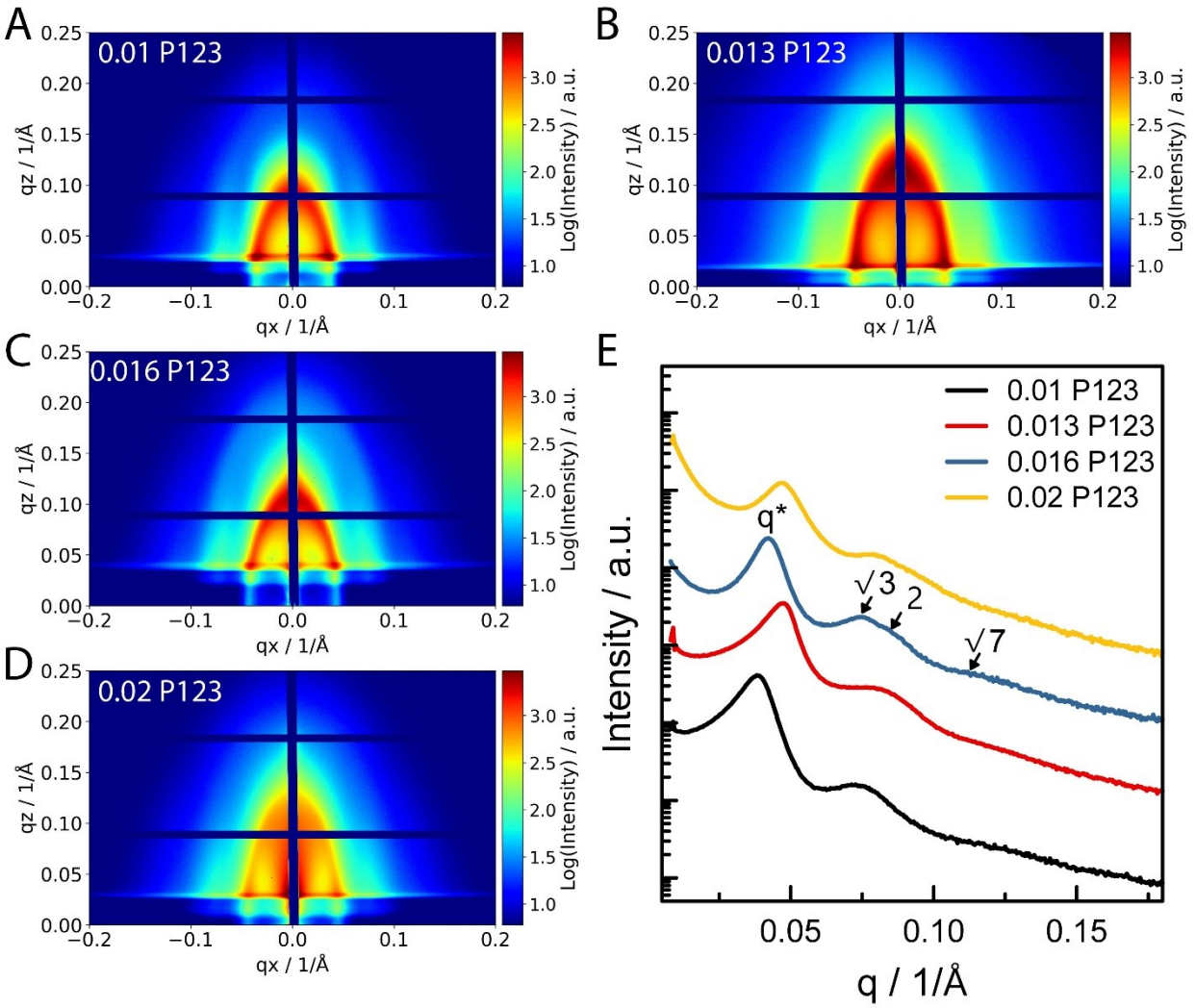

Figure S11: Role of P123 to Modulate Resulting PiRO Alumina Film Structure 2D GISAXS patterns (A-D) for PiRO films with varying ratios porogen amounts to form worm-like chain structures. E) 1D Yoneda band line cuts showing the structural ordering of the films and higher order diffraction peaks labeled for 0.016 P123: Al^{3+}. Films were generated with a 15 min room temperature aging step, 15 minute heated aging at 60 °C and combusted and subsequently annealed at 230 °C for 15 minutes.

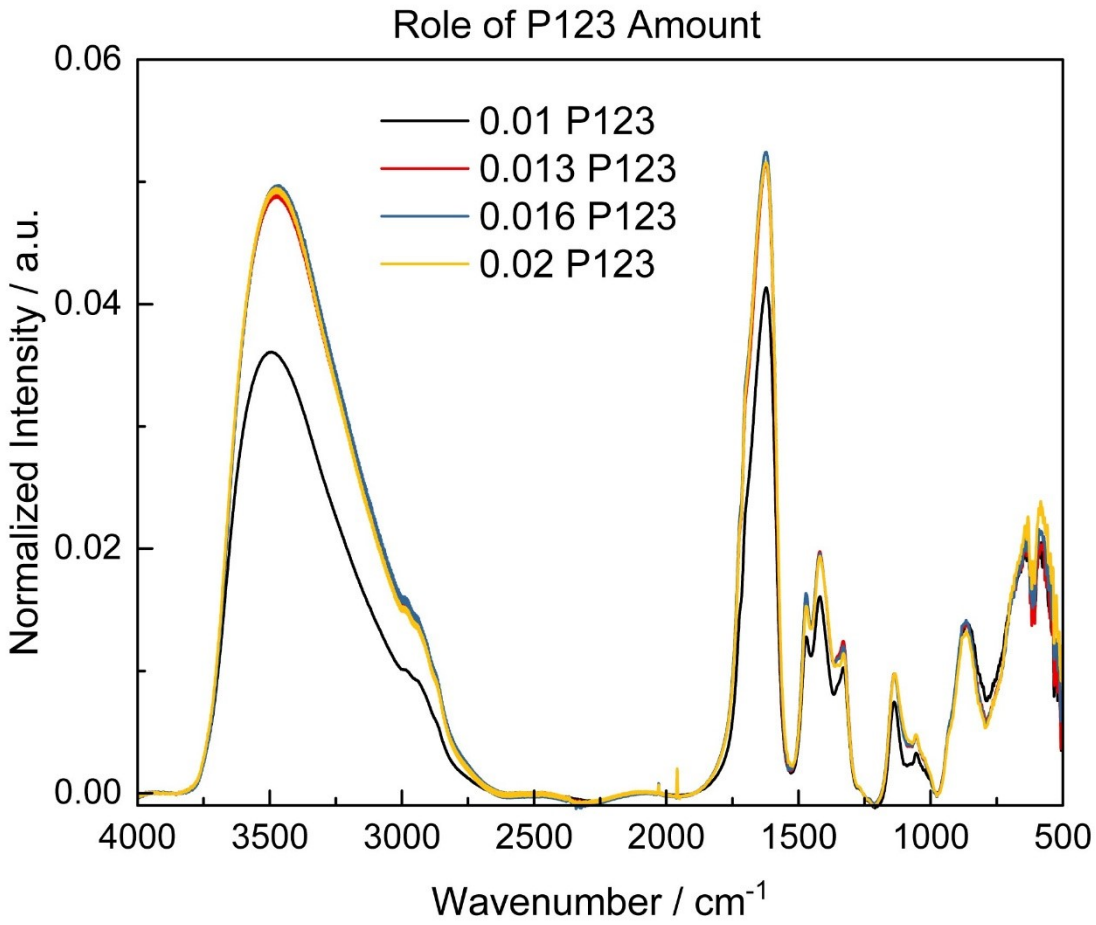

Figure S12: Transmission FTIR of PiRO Films Made with P123 with Varying Precursor Porogen Amount The transmission FTIR shows transmission of the worm-like P123 films made with various P123 loadings with peaks indicating both water and the presence of substantial carbonaceous residue in the films.

Supplementary Section 4: In Situ Thermal Aging of PiRO Alumina with F127

All in situ measurements were performed using the focused beam at SSRL 4-2 SAXS beamline. A monochromated energy of 11 keV and a vacuum pipe beam-to-sample distance of ~1.8 m was used calibrated via silver behenate. The sample stage was mounted on a spindle goniometer via setscrew and positioned at 0.15 deg. incidence. Samples were spin coated in air, carried to the beamline, and measured immediately. Due to the low humidity in the hutch, a standard humidifier was added to assist in obtaining >20% RH. A high-resolution hygrometer (+/- 1%) was used to confirm ambient humidity during measurements (Omega Scientific, HX200HD). For experiments using Adphos, a NIR 50-50 flash curing set-up was used. The Adphos was positioned between the flight path directly above the sample deposited on silicon wafer. The Adphos was remotely operated from outside the hutch by an Arduino Uno and custom circuit in manual mode.

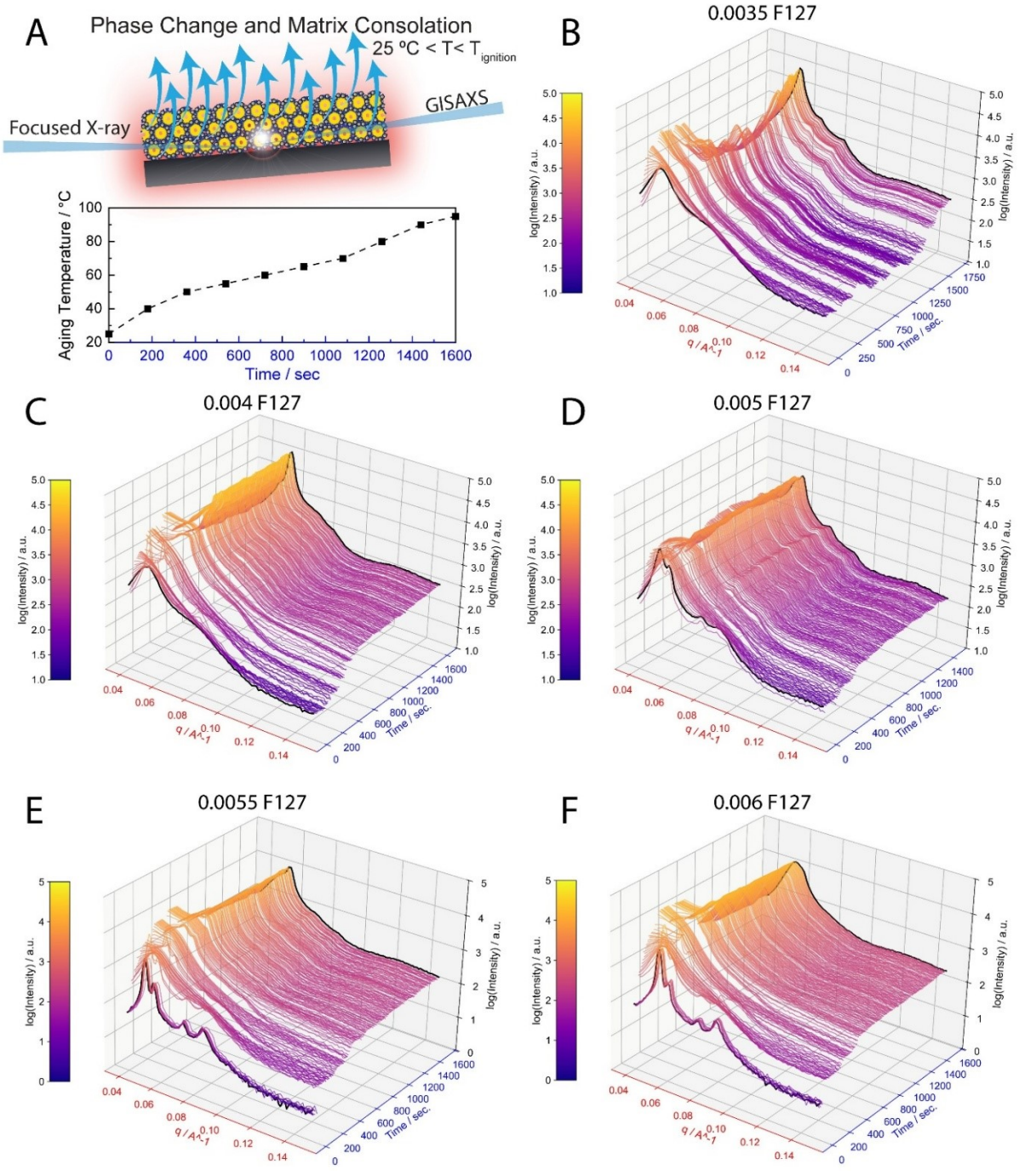

Figure S13: In Situ Self-Assembly of the Deposited PiRO Alumina Precursor as a Function of Annealing and F127 Amount A) A schematic and representative temperature sweep vs. time for the in situ thin film aging, B-F) In situ GISAXS 1D line cuts at the Yoneda band showing structural evolution of alumina precursors containing various amounts of F127 vs. time correlated approximately to the temperature plot in A.

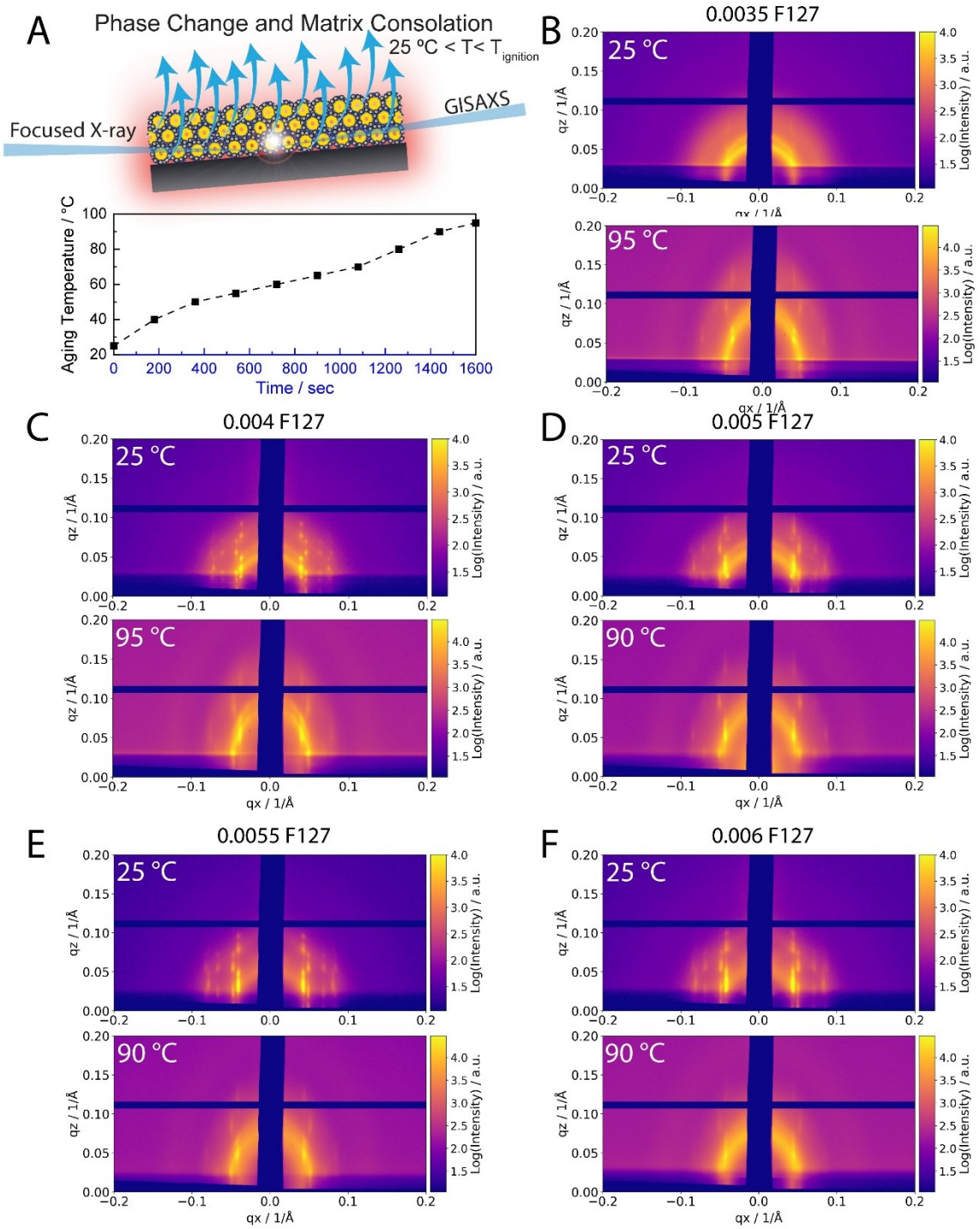

Figure S14: Initial and Final 2D GISAXS PiRO Alumina Precursor as a Function of Annealing and F127 Amount A) A schematic and representative temperature sweep vs. time for the in situ thin film aging, B-F) First and final 2D GISAXS scans for various F127 loadings in PiRO alumina precursors from **Figure S17**.

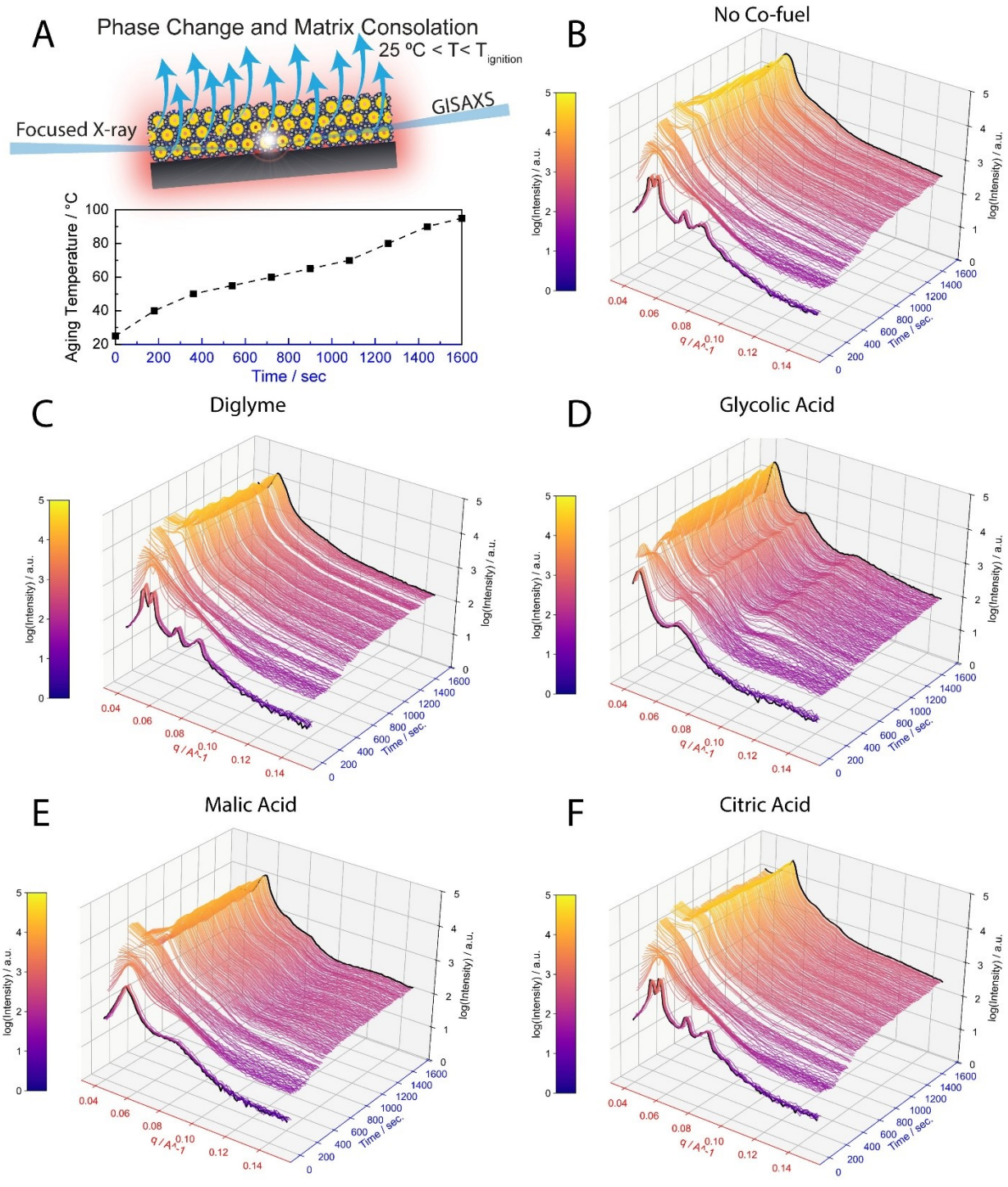

Figure S15: In Situ Self-Assembly of the Deposited F127 PiRO Alumina Precursor as a Function of Annealing and Co-fuel Additive A) A schematic and representative temperature sweep vs. time for the in situ thin film aging, B-F) In situ GISAXS 1D line cuts at the Yoneda band showing structural evolution of alumina precursors containing various small molecule co-fuels at 0.004 F127 : Al^{3+} loading vs. time correlated approximately to the temperature plot in A.

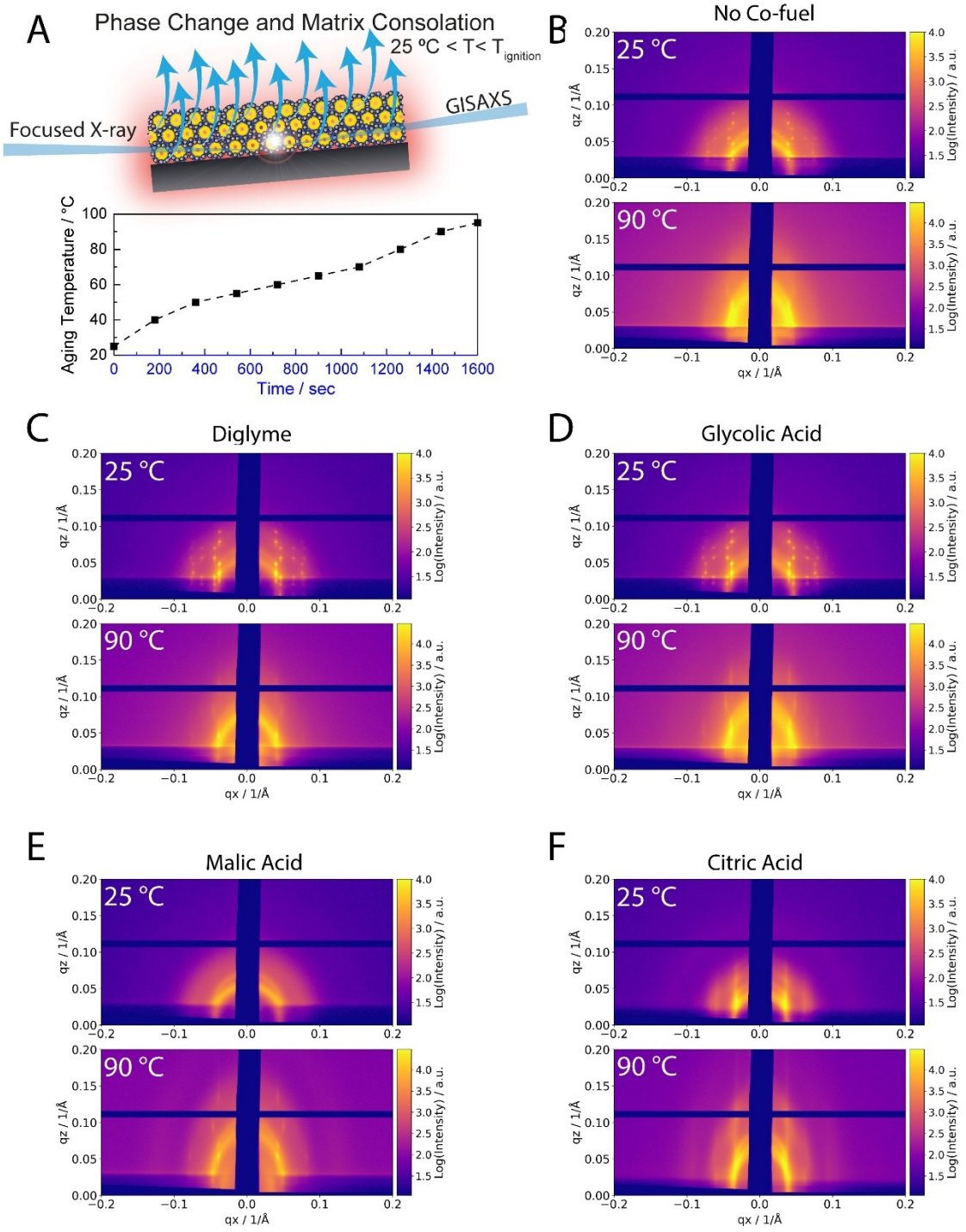

Figure S16: Initial and Final 2D GISAXS F127 PiRO Alumina Precursor with various Co-fuel Additives A) A schematic and representative temperature sweep vs. time for the in situ thin film aging, B-F) First and final 2D GISAXS scans for various co-fuel additives in PiRO alumina precursors from **Figure S19**.

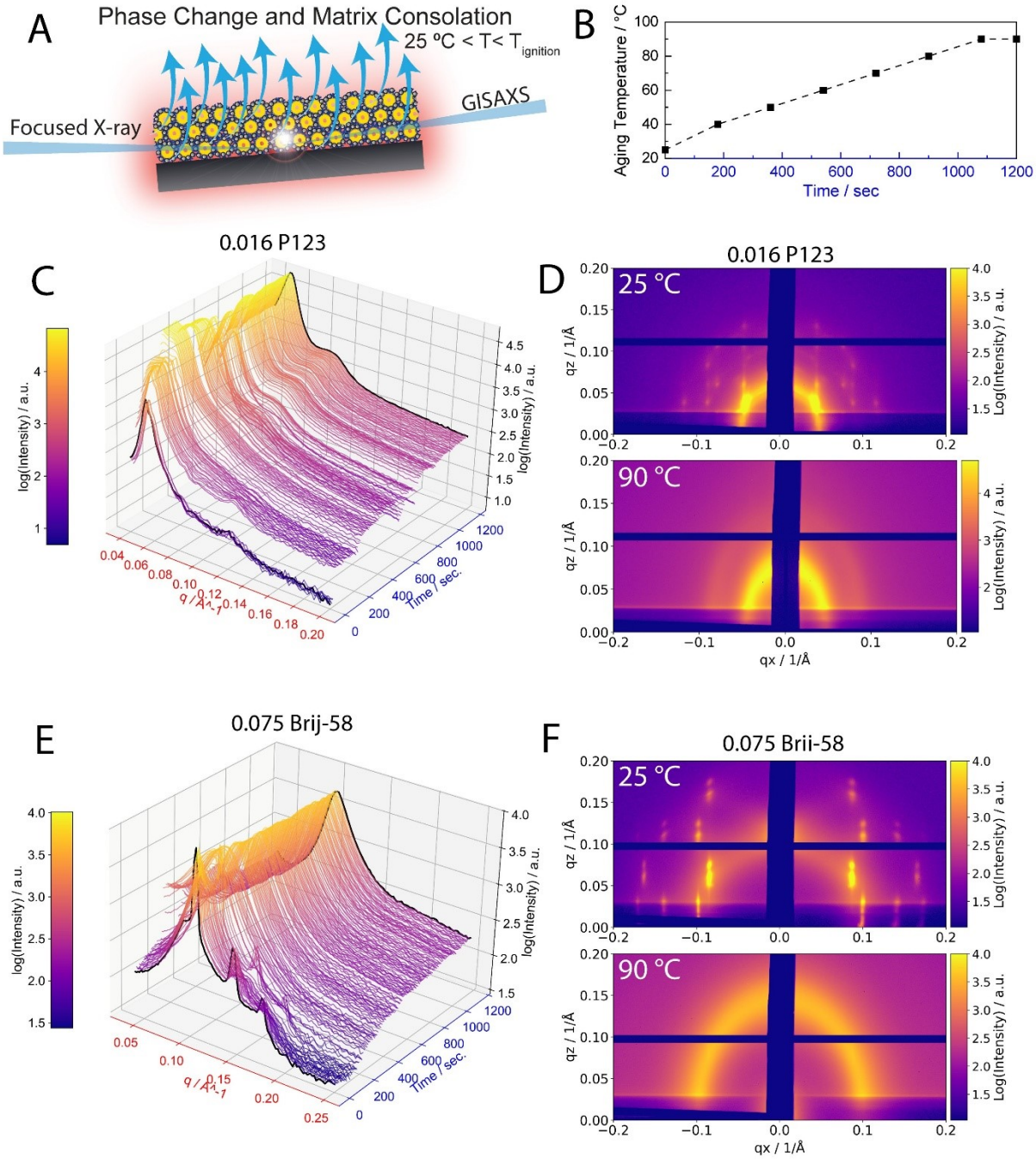

Supplementary Section 5: In Situ Thermal Aging of PiRO Alumina with P123 and Brij-58

Figure S17: In Situ Self-Assembly and Initial and Final GISAXS of the Deposited P123 and Brij-58 PiRO Alumina Precursor as a Function of Annealing Temperature A) In situ beam schematic and B) representative temperature sweep vs. time for the in situ thin film aging. C and E) In situ structural evolution of the Yoneda band vs. annealing temperature for P123 and Brij-58, respectively. D and F) First and final 2D GISAXS scans for the precursor at 25 °C and 90 °C.

Supplementary Section 6: In Situ Combustion of PiRO Alumina with F127

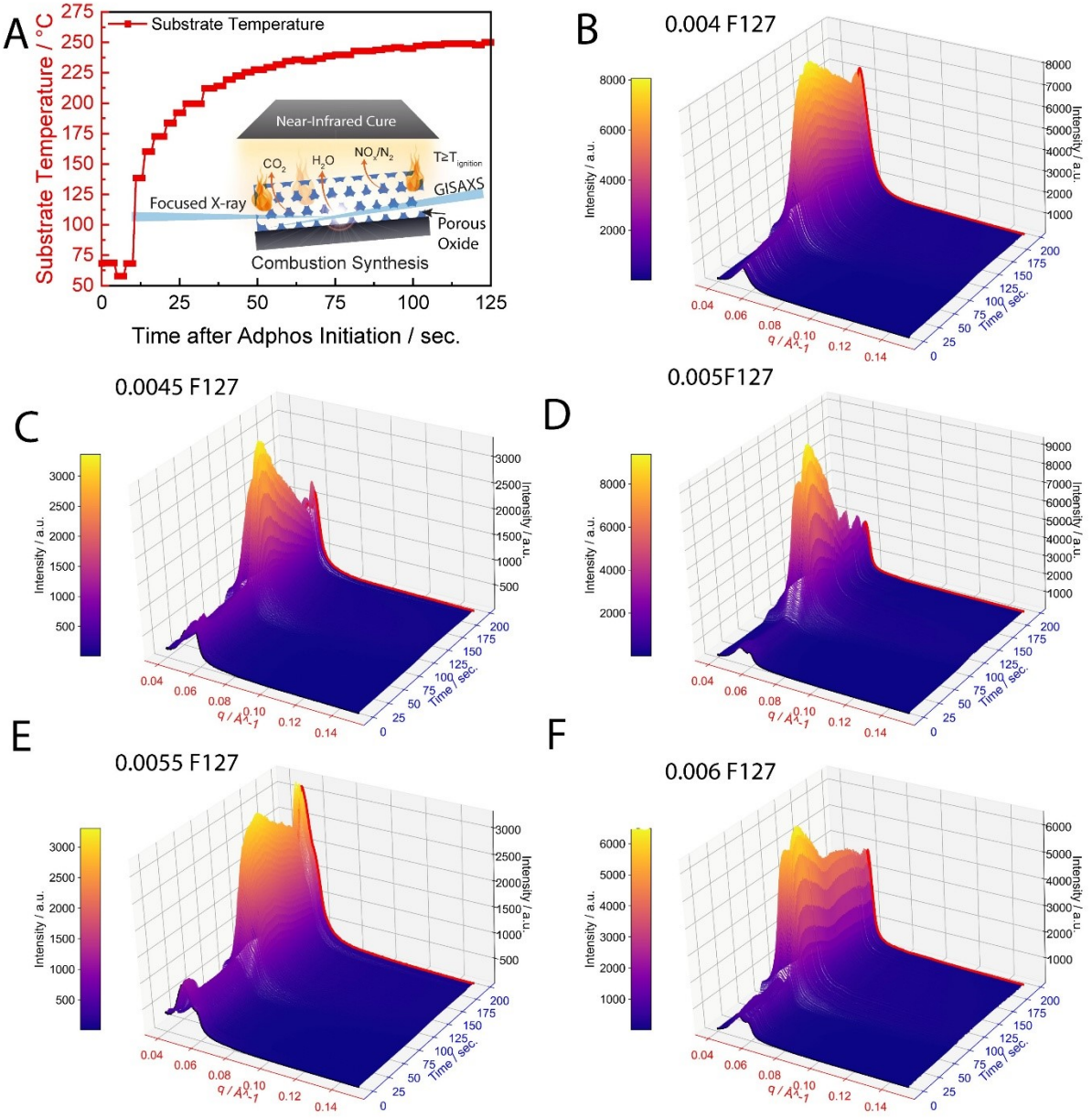

Figure S18: In Situ Combustion under NIR Flash Annealing of PiRO Alumina with Various F127 Precursor Loadings A) In situ beam schematic and representative temperature sweep vs. time for the in situ thin film combustion. B-F) In situ structural evolution of the Yoneda band vs. upon near-IR initiation with approximately 60 seconds without Adphos and two minutes with Adphos on the time axis.

Supplementary Section 7: In Situ Combustion of PiRO Alumina with P123 and Brij-58

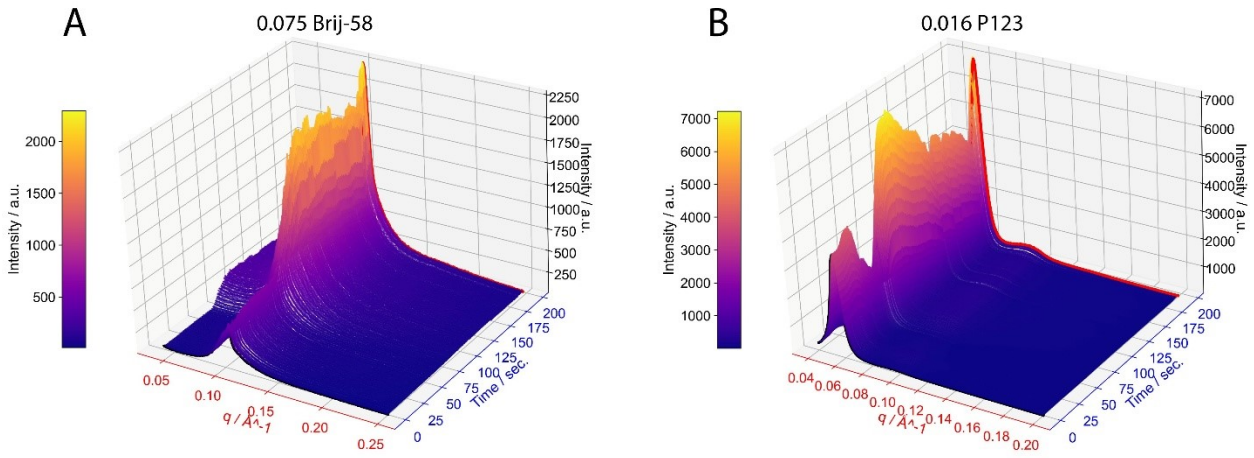

Figure S19: In Situ Combustion under NIR Flash Annealing of PiRO Alumina with P123 and Brij-58 as Structuring Agents A-B) In situ structural evolution of the Yoneda band vs. upon near-IR initiation with approximately 60 seconds without Adphos and two minutes with Adphos on the time axis for A) 0.075 mol Brij-58: Al^{3+} and B) 0.016 mol P123: Al^{3+}.

Supplementary Section 8: In Situ Combustion of Mixed Cation Oxides

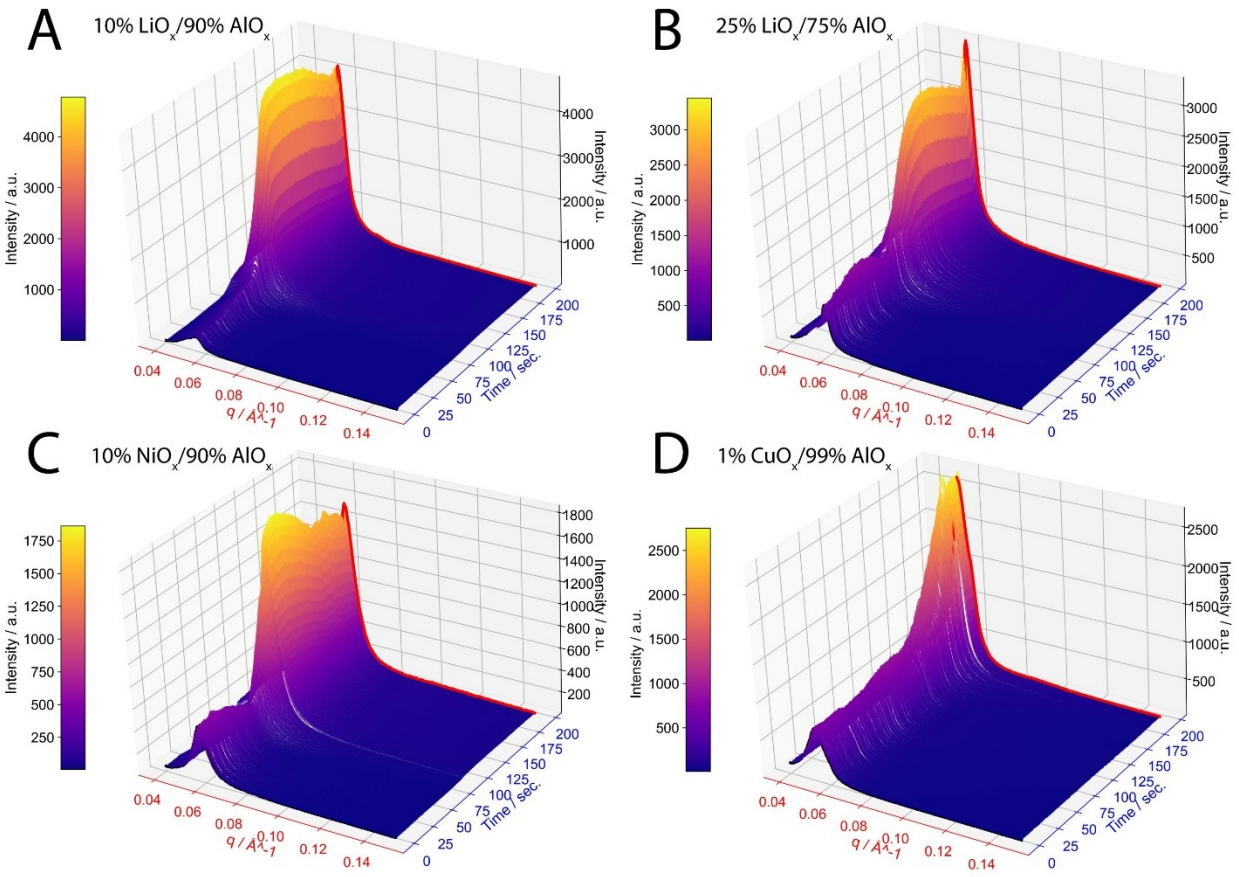

Figure S20: In Situ Combustion under NIR Flash Annealing of Mixed Metal PiRO with 0.004 F127 In situ structural evolution of the Yoneda band vs. upon near-IR initiation with approximately 60 seconds without Adphos and two minutes with Adphos on the time axis for A-B) 10% and 25% Lithiated alumina and C) 10% nickel doped alumina, and D) 1% copper doped alumina.

Supplementary Section 9: Modifying Surfaces of PiRO Alumina Generated with F127 using UV/Ozone and Phosphonic Acid Treatments

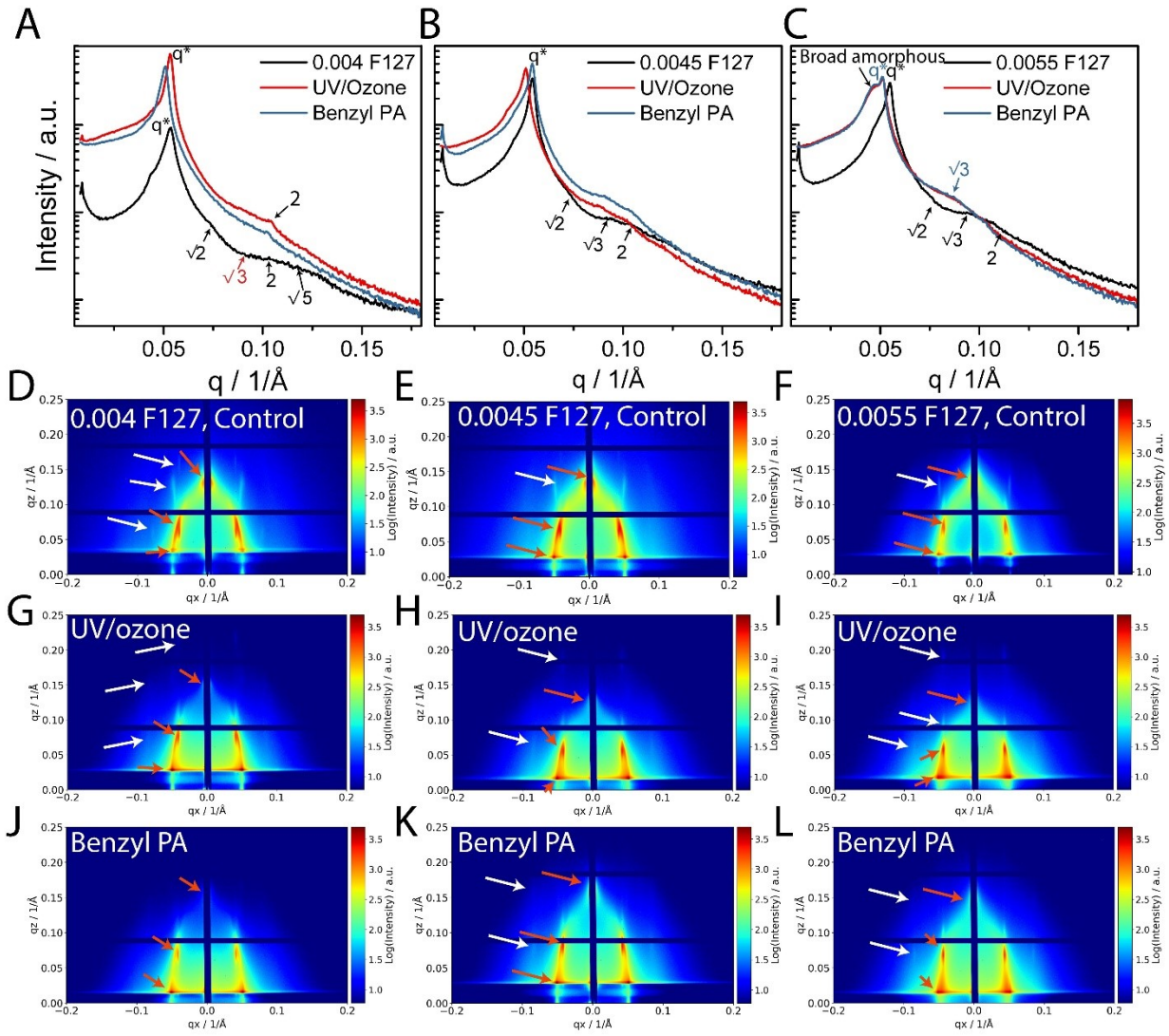

Figure S21: Role of UV/ozone and Phosphonic Acids to Transform PiRO Alumina with Different Precursor Porogen Amounts A-C) Yoneda band line cuts from D-L) 2D GISAXS patterns showing the evolution of structure from as-deposited films (D-F) to post-UV/ozone and post-benzyl PA surface treatment. Orange arrows indicate the main out-of-plane, in-plane, and mixed in- and out-of-plane scattering diffraction spots. White arrows indicate higher diffraction orders. All structures show maintenance of closed-packed scattering as indicated by the diffraction peaks with both qz and qx intensity as well as higher order diffraction peaks. Films were generated with a 15 min room temperature aging step, 15 minute heated aging at 60 °C and combusted and subsequently annealed at 230 °C for 15 minutes. UV/ozone treatment occurred over 15 minutes before PA treatment. For the indexed peaks in A-C, the approximate location is provided with indicated missing peaks in red.

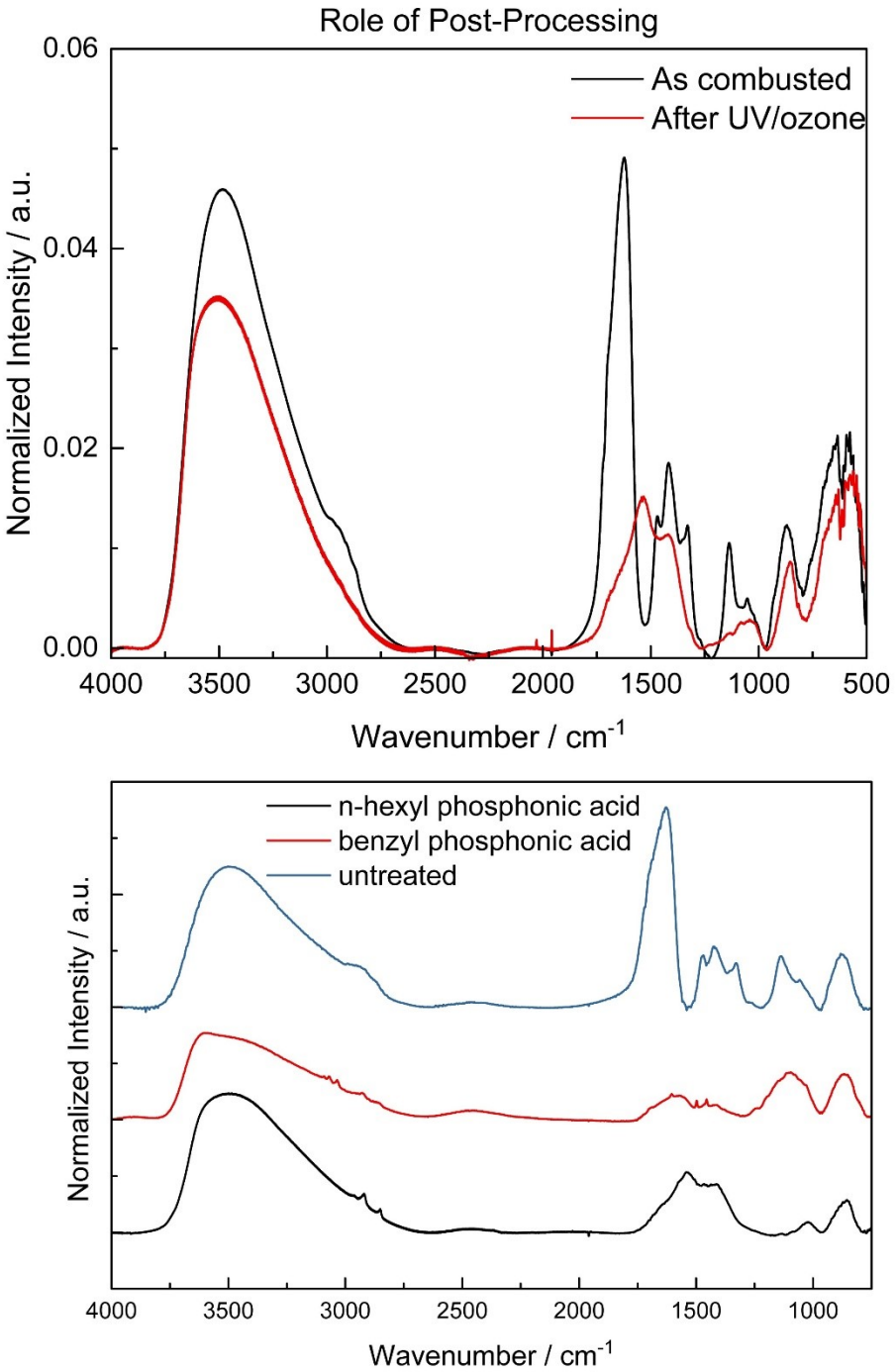

Figure S22: Role of UV/ozone and Phosphonic Acids to Transform PiRO Alumina in Transmission FTIR for F127 Top) Role of UV to remove substantial carbon residue from the thin film as evidenced by loss of common -CH and -CO modes in the film in carboxylic and aliphatic regions as well as a decrease in -OH peak intensity. Bottom) Evolution of the chemical environment in PiRO alumina treated with both n-hexyl and benzyl phosphonic acid showing characteristic aliphatic and benzyl hydrocarbon modes around 3000 cm^{-1} as well as a substantial loss of the carboxylic peak (~1700 cm^{-1}) after ozone exposure.

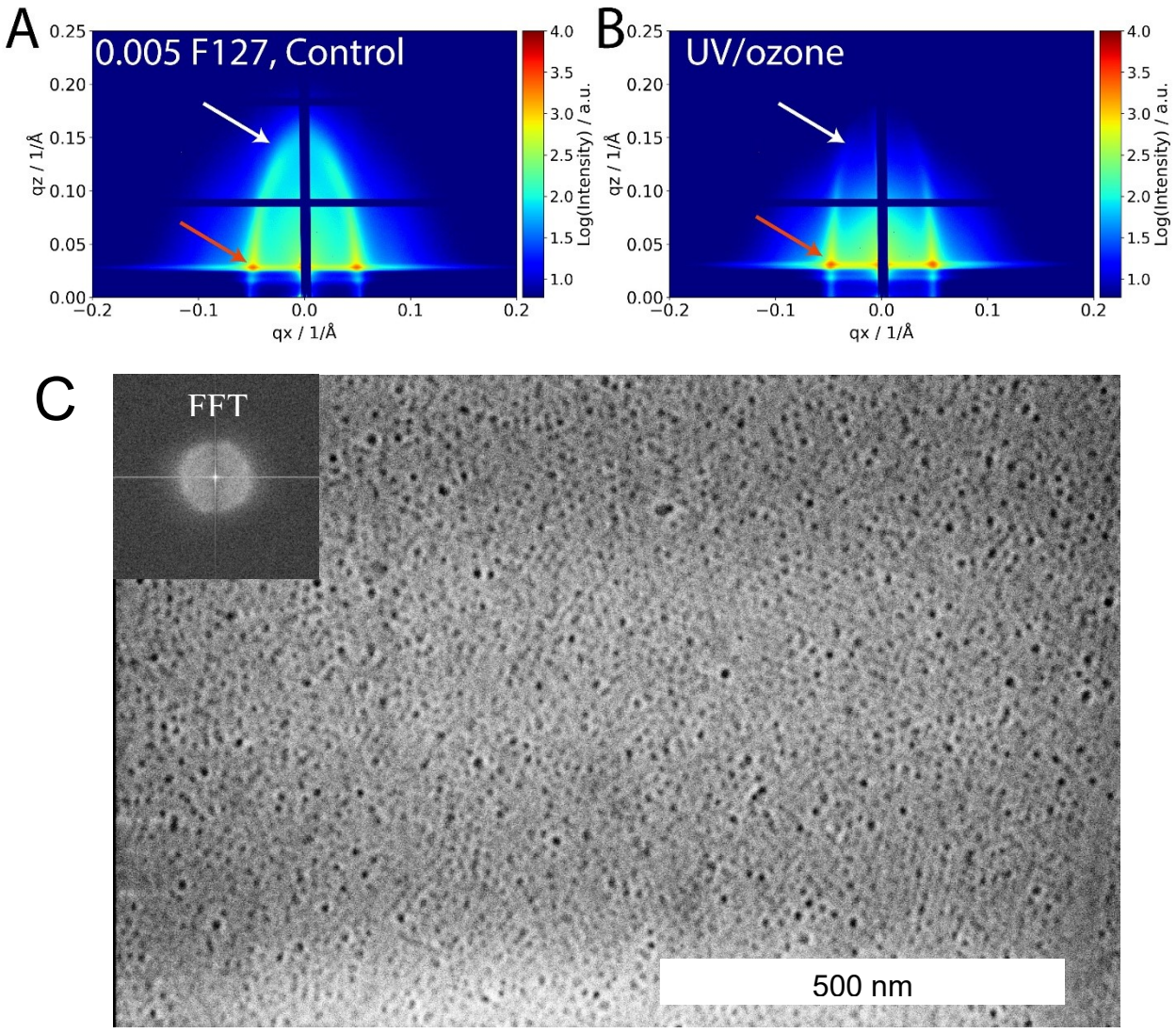

Figure S23: UV/ozone Structural Modification to Transform Vertically Oriented PiRO Alumina Made Via F127 The role of UV/ozone to remove adventitious scattering and result in improved vertical orientation of the Bragg rods as shown by the loss in partial Debye Scherer rings in (A). Films were generated using 0.005 F127:Al^{3+}, with a 15 min room temperature aging step, 15 minute heated aging at 60 °C and combusted and subsequently annealed at 230 °C for 15 minutes. UV/ozone treatment occurred over 15 minutes. Orange arrows indicate the main out-of-plane scattering diffraction spots. White arrows indicate a loss in the Debye-Scherrer disorder after UV/ozone treatment. C) Top-down SEM micrograph and the inset fast-Fourier transform of the image showing the vertically oriented cylindrical pore structure and lack of long-range ordering in the FFT.

Supplementary Section 10: Modifying Surfaces of PiRO Alumina Generated with P123 using UV/Ozone and Phosphonic Acid Treatments

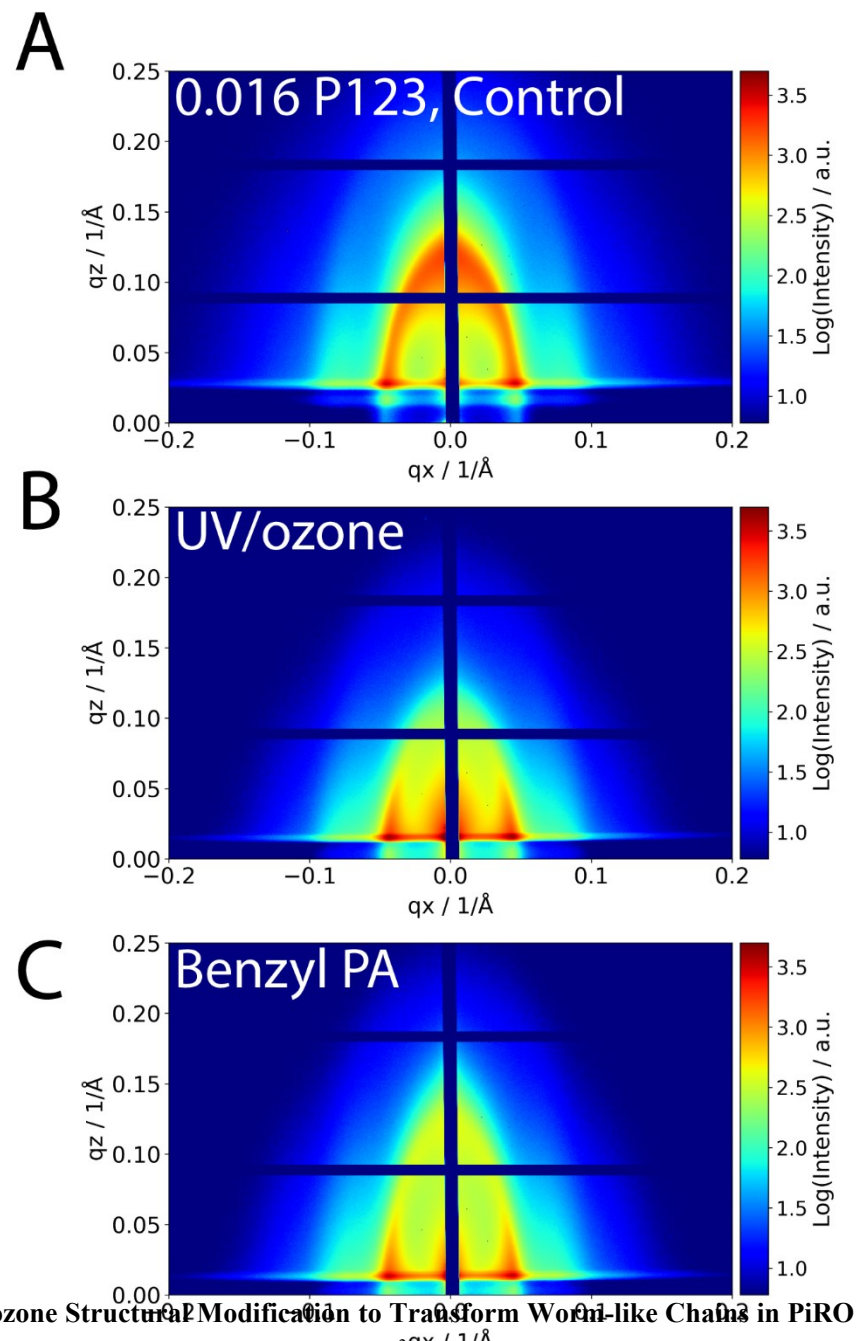

Figure S24: UV/ozone Structural Modification to Transform Worm-like Chains in PiRO Alumina Made Via P123 Films were generated using 0.016 P123:Al[3+], with a 5 min room temperature aging step, 15 minute heated aging at 60 °C and combusted and subsequently annealed at 230 °C for 15 minutes. UV/ozone treatment occurred over 15 minutes.

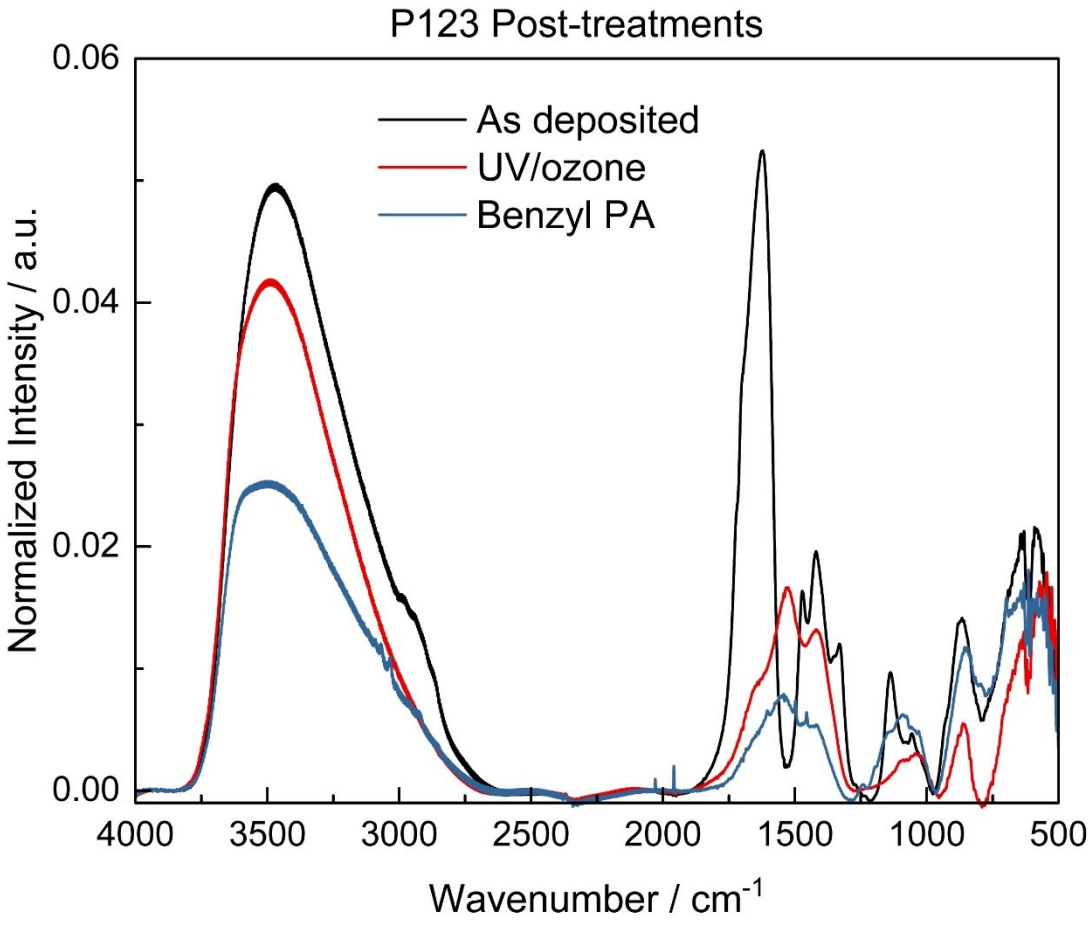

Figure S25: Role of UV/ozone and Phosphonic Acids to Transform PiRO Alumina in Transmission FTIR for P123 As deposited worm-like chains of PiRO alumina made with P123 (Top). Role of UV to remove substantial carbon residue from the thin film as evidenced by loss of common -CH and -CO modes in the film in carboxylic and aliphatic regions as well as a decrease in -OH peak intensity. (Middle) Evolution of the chemical environment in PiRO alumina treated with benzyl phosphonic acid showing characteristic aliphatic and benzyl hydrocarbon modes around 3000 cm^{-1} as well as a substantial loss of the carboxylic peak (~1700 cm^{-1}) after ozone exposure (Bottom).

Supplementary Section 11: Ellipsometry Fits for Oxide Films with Various Porogen Amounts

Table 3: Ellipsometric Fits of The Porous Films from Figure 2

Sample	L1 Thickness (nm)	+/-	L2 Thickness (nm)	+/-	Layer 1 %Void	+/-	Layer 2 %Void	+/-	X^2	Total Thickness (nm)	Avg Porosity (%)
Brij-58 Close-packed	107.6	5.5	211.5	7.9	16.7	0.4	23.6	2.0	3.1	319	21
Brij-58 Vertical Cylinders	100.8	4.6	259.7	16.0	11.1	1.3	36.6	7.4	41.4	361	29
F127 Close-packed	321.7	2.1	105.7	3.5	36.3	0.7	28.4	0.2	0.5	427	34
F127 Vertical Cylinders	16.8	53.5	247.4	53.8	42.3	16.0	36.8	0.3	0.4	264	37
P123 Worm-like Chains	518.1	5.2	-	-	40.6	1.1	-	-	76.5	518	41

This subsequent section of text is directly reproduced from our previous work and represents an identical methodology for measuring porous alumina film properties.[4] A Horiba UVISEL ellipsometer at a 70° incidence angle was used to measure film optical properties from 400-800 nm. To fit the ellipsometric data the thickness of the included layers as well as the porous fraction of each layer were allowed to vary while all other parameters were fixed. The porous fraction is calculated based on the Bruggeman effective medium approximation.[7] The ellipsometric model for measurements of film thickness was validated against profilometry measurements on the same film.

The refractive index (n) of the alumina phase was modelled with the New Amorphous model, an adaption of the Forouhi-Bloomer formulation.[8] The parameters (all in eV) are f_j, the strength of the extinction coefficient, Γ_j, the broadening at peak absorption, ω_j, the location of the extinction coefficient maxima, and ω_g, the material bandgap. Values for alumina were: $f_j = 2.46$ eV, $\Gamma_j = 0.44$ eV, $\omega_j = 10.4$ eV, $\omega_g = 9.85$ eV. For void space, the $n = 1$. The properties of the alumina and void were fixed and the only parameters allowed to vary were the layer thickness and the porosity.

Supplementary Section 12: X-ray Photoelectron Spectroscopy (XPS) of Bimetallic Ni/Al and Cu/Al Oxides

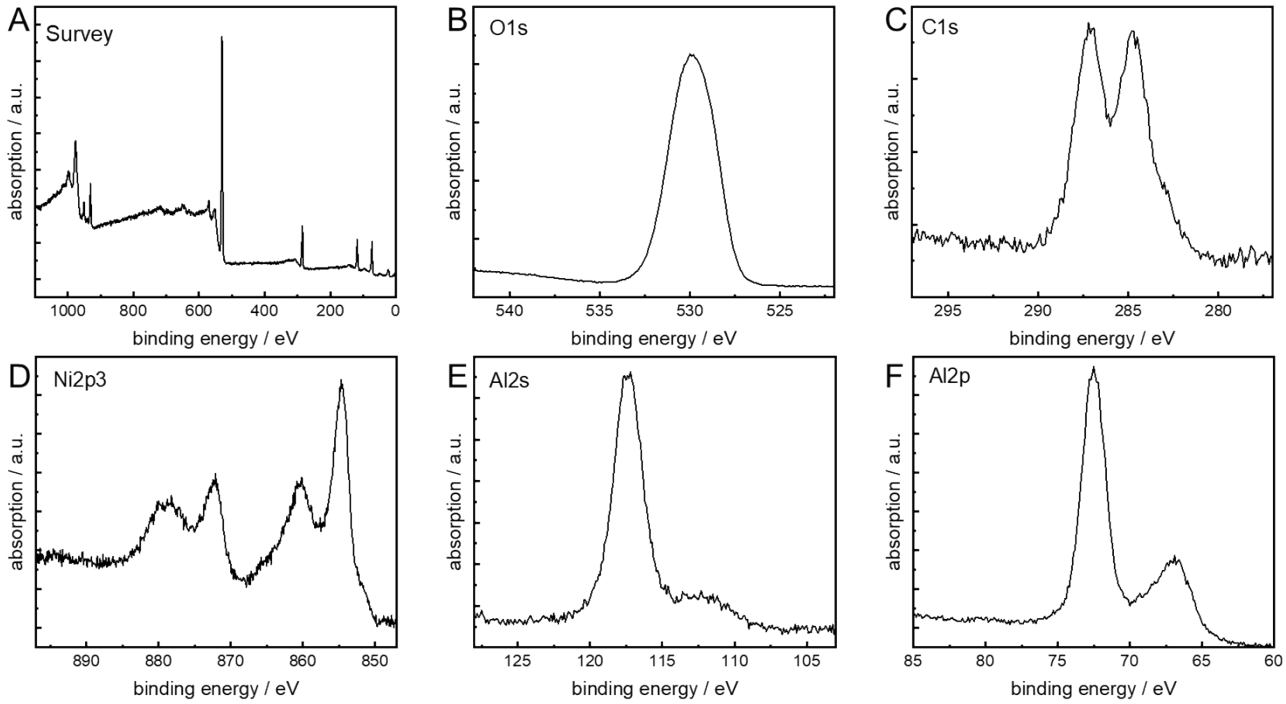

Figure S26: Survey and High-resolution XPS of thin film nickel aluminum oxide Surface XPS showing the composition of the surface of 10% Ni and AlO_x showing the overall survey (A), oxygen 1s (B), carbon 1s (C), nickel 2p (D), aluminum 2s (E), and aluminum 2p (F). The C-H peak was shifted to a binding energy of 284.8 eV and charge neutralizers were used.

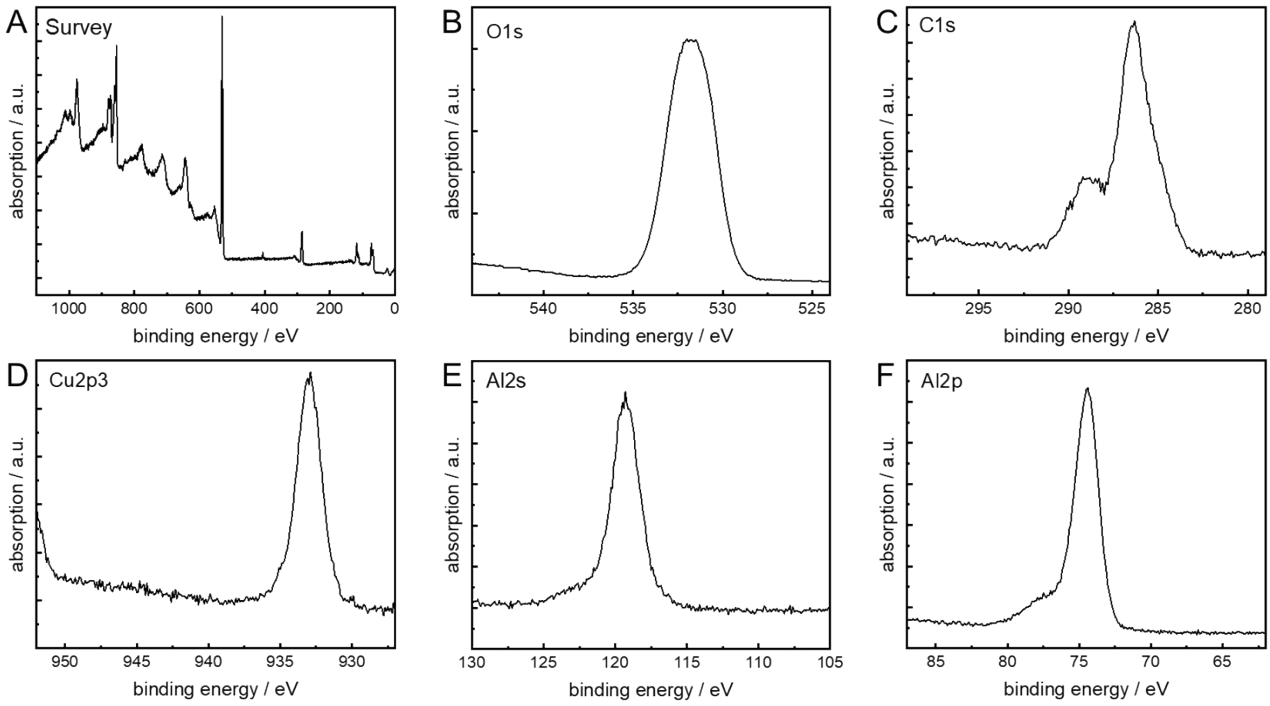

Figure S27: Survey and High-resolution XPS of thin film copper aluminum oxide Surface XPS showing the composition of the surface of 10% Cu and AlO_x showing the overall survey (A), oxygen 1s (B), carbon 1s (C), copper 2p3 (D), aluminum 2s (E), and aluminum 2p (F). The C-H peak was shifted to a binding energy of 284.8 eV and charge neutralizers were used.

Table 4: Peak Fits from High Resolution XPS

Element	10% Cu in AlO_x	10% Ni in AlO_x
O1s	52 at%	53 at%
C1s	25 at%	14 at%
Al2p	19 at%	24 at%
Cu2p3	3 at%	-
Ni2p3	-	8 at%
N1s	0 at%	1 at%
Total (at%)	100 at%	100 at%

The film surfaces with high resolution XPS peaks were fit to give compositional fits and the peak shifts for nickel, copper, aluminum, oxygen, carbon, and nitrogen. The films show high carbon loading as commonly observed on PiRO film surfaces. Depth profiling with argon sputtering is known to reduce transition metals like nickel so it was avoided.

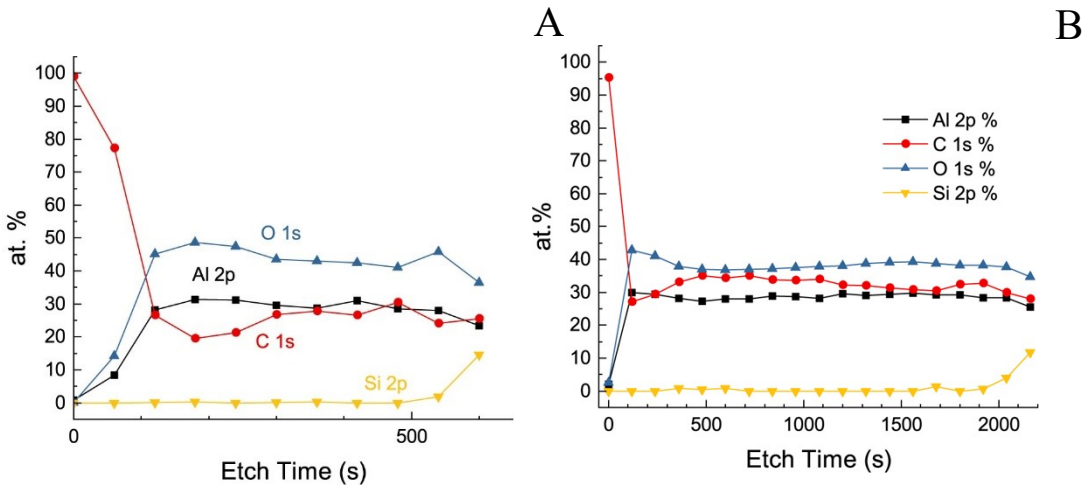

Figure S28: Nanocomposite structure generated from PiRO alumina filled with TOPAS® Polyolefin and Polystyrene XPS depth profiling (A) showing the TOPAS (C1s peak) filling the PiRO alumina matrix and (B) Polystyrene filling of PiRO alumina matrix.

Supplementary Works Cited

[1] J. Liu, K. G. Yager, *IUCrJ* **2018**, *5*, 737.
[2] J. A. Steele, E. Solano, D. Hardy, D. Dayton, D. Ladd, K. White, P. Chen, J. Hou, H. Huang, R. A. Saha, L. Wang, F. Gao, J. Hofkens, M. B. J. Roeffaers, D. Chernyshov, M. F. Toney, *Advanced Energy Materials* **2023**, *13*, 2300760.
[3] J. M. Calo, P. J. Hall, *Carbon* **2004**, *42*, 1299.
[4] D. W. Collinson, T. W. Colburn, R. D. Miller, R. H. Dauskardt, *Advanced Materials* **2025**, *37*, 2504719.
[5] P. Müller-Buschbaum, in *Applications of Synchrotron Light to Scattering and Diffraction in Materials and Life Sciences* (Eds.: M. Gomez, A. Nogales, M. C. Garcia-Gutierrez, T. A. Ezquerra), Springer, Berlin, Heidelberg, **2009**, pp. 61–89.
[6] "GISAXS," can be found under https://www.classe.cornell.edu/~dms79/gisaxs/GISAXS.html, **n.d.**
[7] C. Boissiere, D. Grosso, S. Lepoutre, L. Nicole, A. B. Bruneau, C. Sanchez, *Langmuir* **2005**, *21*, 12362.
[8] A. R. Forouhi, I. Bloomer, *Phys. Rev. B* **1986**, *34*, 7018.